Signal Quality Analysis in Pulse Oximetry: Modelling and Detection of Motion Artifact

by

Geoffrey Clarke, **B.Eng.**

A thesis submitted to the

Faculty of Graduate and Postdoctoral Affairs

in partial fulfillment of the requirements for the degree of

Master of Applied Science in Biomedical Engineering

Ottawa-Carleton Institute for Biomedical Engineering

Department of Systems and Computer Engineering

Carleton University

Ottawa, Ontario

May 2015

The undersigned hereby recommends to the

Faculty of Graduate and Postdoctoral Affairs

acceptance of the thesis

Signal Quality Analysis in Pulse Oximetry: Modelling and Detection of Motion Artifact

submitted by **Geoffrey Clarke**, **B.Eng.**

in partial fulfillment of the requirements for the degree of

Master of Applied Science in Biomedical Engineering

Professor Adrian D.C. Chan, Thesis Co-Supervisor

Professor Andy Adler, Thesis Co-supervisor

Professor Roshdy Hafez, Chair,
Department of Systems and Computer Engineering

Ottawa-Carleton Institute for Biomedical Engineering

Department of Systems and Computer Engineering

Carleton University

May, 2015

Abstract

Pulse oximetry is a non-invasive technique for measuring the amount of oxygen in a patient's arterial blood, as a percentage of the blood's oxygen carrying capacity (SpO_2). This measurement is considered standard of care in the hospital for monitoring the cardio-respiratory function of a patient. While it has potential uses in ambulatory or wearable monitoring applications, pulse oximetry is particularly susceptible to motion artifact contamination. This thesis presents efforts to quantify and model the effects of motion artifact, and automatically detect periods of poor signal quality.

First, the effects of motion artifact on SpO_2 are analyzed using motion contaminated data. Second, two models are identified from previous literature that may explain the effects of motion artifact on pulse oximetry. These models are developed analytically and evaluated using isolated motion artifact signals. Finally, three automatic signal quality assessment algorithms are proposed. These algorithms are shown to discriminate between clean and motion contaminated signals.

Overall, this thesis attempts to inform the development of software and hardware based techniques to mitigate the effects of poor signal quality on pulse oximetry.

Acknowledgments

I would like to express my gratitude to my supervisors, Dr. Adrian Chan and Dr. Andy Adler for their continuous support of my studies. Their expertise, mentorship and patience provided for a fantastic graduate experience.

To my colleagues Patrick Quesnel and Chris Andison, thank you for your brainstorming, debates, and editorial assistance. I look forward to working with you in the future. Thanks to Kait Duncan for your support and editorial assistance, and for making me dinner sometimes, even though you're busier than me. Despite your patience, I'm sure you're as happy as I am that I'm done!

Finally, I am grateful to my family, who have always taken interest in my academic progress. Thank you for your unwavering support, patience, and encouragement to take on this endeavour in the first place.

Statement of Originality

This thesis presents the work of the author, under the supervision of Dr. Adrian D. C. Chan and Dr. Andy Adler. This work was completed at Carleton University for the degree Master of Applied Science in Biomedical Engineering. Some of these results have been or will be presented in conference publications:

1. G. W. J. Clarke, A. D. C. Chan, and A. Adler, "Effects of motion artifact on the blood oxygen saturation estimate in pulse oximetry," *2014 IEEE International Symposium on Medical Measurements and Applications (MeMeA)*, pp. 14, 2014.

    - This conference paper describes the initial work in quantifying the effect of motion artifact in pulse oximetry. This work was expanded upon in Chapter 4, using an improved blood-oxygen saturation calculation algorithm, and comparing to a contaminant free reference signal recorded in parallel. This paper was presented by the author at the 2014 IEEE International Symposium Medical Measurements and Applications (MeMeA).

2. G. W. J. Clarke, A. D. C. Chan, and A. Adler, "Quantifying Blood-Oxygen Saturation Measurement Error in Motion Contaminated Pulse Oximetry Signals," *World Congress on Medical Physics and Biomedical Engineering*, 2015.

    - This conference paper describes the collection of isolated motion artifact signals, allowing for artificial signal contamination with precise control over

signal to noise ratio. The measurement error of the conventional pulse oximetry algorithm is calculated over a range of signal to noise ratios. The results of this paper are found in Chapter 4, and will be presented by the author at the 2015 World Congress on Medical Physics and Biomedical Engineering.

Table of Contents

List of Tables

List of Figures

Abbreviations

ε	Optical extinction coefficient of a transmission medium
AC	Alternating current - the varying component of a signal
ADC	Analog to digital converter
AFE4400	Texas Instruments analog front end for pulse oximetry
BPM	Beats per minute - expression of heart rate
DAC	Digital to analog converter
DC	Direct current - the non-changing baseline component of a signal
Hb	Haemoglobin - the oxygen transport molecule in the blood
HbO_2	Oxygenated haemoglobin
LED	Light-emitting diode
PPG	Photoplethysmograph - volume measurement based on light absorption
R	The ratio of ratios parameter used to calculate SpO_2
RMS	Root-mean-square amplitude of a signal
SaO_2	Arterial blood-oxygen saturation, expressed as a percentage
SNR	Signal to noise ratio, expressed in decibels (dB)
SpO_2	Arterial blood-oxygen saturation measured by pulse oximetry
SQI	Signal quality index

Chapter 1

Introduction

Healthcare systems around the world are being challenged by increasing costs and demand for services. Most developed countries have seen their healthcare costs rise as a percentage of GDP in the past decade [1]. There is an increasing need to ease the pressure on healthcare systems by moving health monitoring out of the hospital and into the home. Advances in telemedicine and portable technology may offer a solution to this problem [2, 3].

Typical medical monitoring devices found in a hospital require interaction with a trained practitioner in a controlled environment to ensure clinically relevant measurements. Performing an electrocardiogram (ECG), electromyogram (EMG), electroencephalogram (EEG), blood pressure measurement or blood-oxygen saturation measurement require patient preparation and equipment setup. Patients are often required to remain still and quiet while tests are being performed. All of these devices require a clinician to process signals or alarms, assess the quality of the information, and decide how to direct patient care based on that information.

Despite the care taken by the clinician, tests performed in the hospital are only a snapshot, and may not capture issues that only occur occasionally. This issue demonstrates the potential benefits to medical monitoring in a continuous fashion. A

patient's condition can be assessed during their regular daily routines, and significant events can be captured that may have been missed in the hospital.

Many developers of wearable health technology target the consumer electronics market with fitness tracking devices. This has lead to an explosion of wearable devices measuring heart rate, respiration rate, oxygen saturation, activity levels and sleep quality [4].

There are benefits to this approach - companies are able to develop technology for the consumer market without the cost of medical device licensing. However, the common thread still exists - these are medical devices, and have the potential to provide valuable data to a patient's electronic health record without a hospital visit.

When monitoring moves into unsupervised environments, the quality and interpretation of collected data can come into question. Clinicians may not be available to supervise the use of continuous devices or act on alarms. Furthermore, ambulatory monitoring is subject to motion artifact - signal noise caused by movement of the patient. This may degrade the quality of the data being recorded.

To guide the advancement of wearable medical devices, it is helpful to look at the state of existing technology in the hospital versus the consumer electronics market. Pulse oximetry - a technique for evaluating a patient's cardio-respiratory function - is considered standard of care in the operating room and intensive care units, yet it has been largely neglected in the consumer health space. A pulse oximeter estimates a patient's arterial blood-oxygen saturation (SaO_2) non-invasively, and reports this estimate as the peripheral capillary oxygen saturation (SpO_2).

1.1 Motivation

Pulse oximetry may be facing slow adoption in consumer devices due to its sensitivity to motion artifact. Previous work demonstrates a decrease in measurement accuracy and an increase in false alarms for hypoxia (low blood oxygen saturation) in the presence of motion artifact [5, 6].

Despite the importance of measuring SpO_2 in the hospital, and its possible applications in ambulatory environments, sensitivity to motion artifact makes pulse oximetry ill suited to portable or wearable monitoring applications.

1.2 Biosignal Quality Analysis

In controlled environments, expert operators can manually detect poor quality biosignals and intervene to correct the problem. As medical devices leave controlled environments and enter remote monitoring applications, the importance of automatic signal quality analysis becomes fundamental [3]. For pulse oximetry in particular, [3] notes that despite research into mitigation of motion artifact, little has been done to address the cases where signal quality is so poor that useful data cannot be extracted.

Automatic biosignal quality analysis can be divided into four fundamental problems: detection of a signal contaminant, identification of the type of contaminant, quantification of the contaminant's effect on the signal, and mitigation [7]. This work seeks to address some of the gaps in detection and quantification of motion artifact in pulse oximetry, with the goal of masking the signals where artifact mitigation is unfeasible.

1.3 Objectives

The objective of this work is to gain understanding of the signal quality challenges facing ambulatory pulse oximetry monitoring. Specifically, this thesis seeks to:

1. Quantify the effect of motion artifact on pulse oximetry signals.
2. Define and evaluate pulse oximetry motion artifact models proposed in the literature.
3. Develop and evaluate multiple automatic signal quality assessment algorithms to detect motion artifact and other signal quality issues in pulse oximetry.

1.4 Contributions

The following contributions are presented in this thesis:

Evaluation of measurement error in motion contaminated pulse oximetry

Previous work has demonstrated measurement error associated with motion artifact in pulse oximetry [5,6]. The size of this error is highly dependent on the parameters of the specific SpO_2 calculation algorithms employed. Chapter 4 evaluates measurement bias and variance in a set of motion contaminated signals using the conventional SpO_2 calculation algorithm. These parameters are also evaluated as a function of signal to noise ratio in artificially contaminated signals.

Analytical modelling of pulse oximetry motion artifact

Explanations for the effects of motion artifact on pulse oximetry are hypothesized in the literature [8], but with little supporting evidence. Chapter 5 re-derives the SpO_2

algorithm to include these effects, and discusses the predicted effect of motion artifact on SpO_2 calculation. The models are evaluated using isolated motion artifact signals.

Development and evaluation of automatic signal quality assessment

If poor quality signals can be identified and ignored, the measurement error associated with motion artifact can be mitigated. Chapter 6 proposes three simple signal quality assessment algorithms, and evaluates their performance using real and artificial motion contaminated signals.

Portions of this work have been disseminated in the following papers:

- G. W. J. Clarke, A. D. C. Chan, and A. Adler, "Effects of motion artifact on the blood oxygen saturation estimate in pulse oximetry," *Medical Measurements and Applications (MeMeA), 2014 IEEE International Symposium on*, pp. 14, 2014. [9]

- G. W. J. Clarke, A. D. C. Chan, and A. Adler, "Quantifying Blood-Oxygen Saturation Measurement Error in Motion Contaminated Pulse Oximetry Signals," *World Congress on Medical Physics and Biomedical Engineering*, 2015. [10]

1.5 Thesis Organization

The remainder of this document is structured as follows:

Chapter 2: Provides a literature review of the basic principles of pulse oximetry. This includes a discussion of the development of the technology up to the current research in motion-resistant and calibration-free pulse oximetry. Gaps in the current body of knowledge are identified.

Chapter 3: Describes the data acquisition equipment and methodology used to collect a dataset for this study. Additionally, the development of the digital algorithm to calculate SpO_2 from raw PPG signals is discussed.

Chapter 4: Explores the effects of motion artifact on SpO_2 data. Measurement accuracy and precision are quantified using real contaminated PPG signals and artificially contaminated data.

Chapter 5: Presents possible models to explain motion-induced SpO_2 hypoxia alarms. These models are evaluated by characterizing real isolated motion artifact signals.

Chapter 6: Details the development of multiple SpO_2 signal quality analysis algorithms. These algorithms are evaluated for their ability to identify and quantify motion artifact in real and artificially contaminated PPG signals.

Chapter 7: Presents the conclusions of the research and provides recommendations for future work.

Appendix A: Provides a derivation of the SpO_2 calculation from the Beer-Lambert law of light absorption.

Appendix B: Provides raw data for the signal quality index (SQI) calculations in Chapter 6.

Chapter 2

Background

This chapter provides a review of the principles of pulse oximetry and the latest research reported in the literature. Section 2.1 provides an introduction to pulse oximetry measurement. Section 2.2 discusses clinical and non-clinical applications of pulse oximetry. Section 2.3 reviews previous efforts to understand the effects of motion artifact and develop automatic signal quality assessment. Section 2.4 describes today's state of the art research in pulse oximetry technology.

2.1 Introduction to Pulse Oximetry

2.1.1 Oxygen Transport

Oxygen is a key ingredient in cellular respiration - the chemical processes by which human cells generate energy. In normal human respiration, oxygen is first diffused across the alveolar-capillary membrane from the lungs into the bloodstream. This process is illustrated in Fig. 2.1. Oxygen molecules bind to haemoglobin (Hb) - the main carrier of oxygen in the blood. Each haemoglobin protein can carry four oxygen molecules.

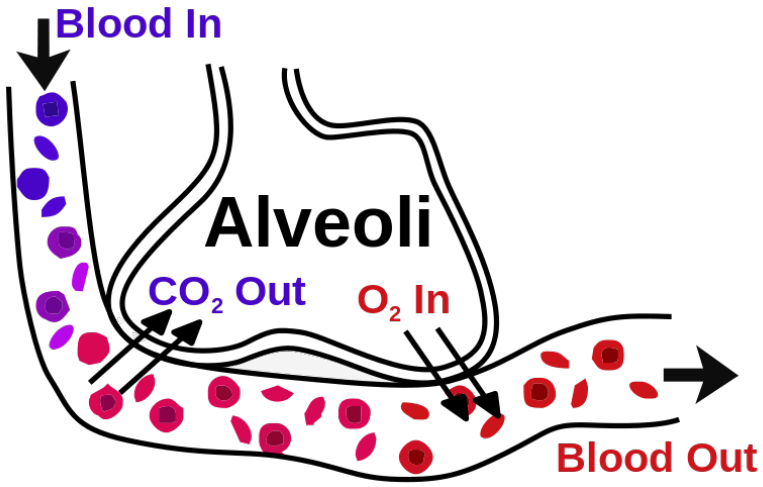

Figure 2.1: Gaseous exchange in the lung (Reproduced from [11]).

There are four species of haemoglobin found in healthy adult blood:

- Oxyhaemoglobin (HbO_2) is completely saturated with oxygen.
- Deoxyhaemoglobin (Hb) is not completely saturated with oxygen.
- Methaemoglobin (MetHb) is an altered form of haemoglobin, and is unavailable for oxygen transport.
- Carboxyhaemoglobin (COHb) is saturated with carbon monoxide, and is unavailable for oxygen transport.

The first two species (HbO_2 and Hb) are functional haemoglobins, and are either transporting or are capable of transporting oxygen. Dysfunctional haemoglobins (MetHb and COHb) are not available for oxygen transport, and make up 1-2% of the total haemoglobin molecules in a healthy, non-smoking adult [12].

In the arterial blood of a healthy person, greater than 95% of the total haemoglobin molecules are carrying oxygen. This figure is known as arterial blood-oxygen saturation, or SaO_2, and is defined in (2.1) where $[HbO_2]$, $[Hb]$, $[metHb]$ and $[COHb]$ are the concentrations of oxy-, deoxy-, met- and carboxy- haemoglobin, respectively.

$$SaO_2 = \frac{[HbO_2]}{[HbO_2] + [Hb] + [metHb] + [COHb]} \times 100\% = \frac{[HbO_2]}{[TotalHb]} \times 100\% \quad (2.1)$$

Oxygen transport can be modelled as a simple supply and demand problem; if the oxygen demand from the tissues exceeds the lungs' capacity to supply it, SaO_2 decreases. This condition of oxygen deprivation is known as hypoxia. Conditions that limit the supply of oxygen include lung injury, airway injury or low partial pressure of oxygen in the air. Healthy patients under general anaesthesia can experience reduced respiratory drive, which can also limit the supply of oxygen during surgery. Conditions increasing the demand for oxygen include intense exercise, fever and infection. In surgery and intensive care, SaO_2 is standard of care in assessing respiratory function and diagnosing hypoxia.

SaO_2 is measured using arterial blood gas analysis. This test involves sampling blood from an artery and sending it to a lab oximeter, which uses spectroscopic techniques to distinguish all four species of haemoglobin. However, this technique is ill suited to emergency situations - it requires several minutes to process the sample and obtain the results. The time delay and the invasive nature of this procedure necessitate an alternative that is both non-invasive and better suited to continuous monitoring.

2.1.2 Measuring SpO_2 with Pulse Oximetry

SaO_2 is a direct, invasive measurement of the oxygen content of the blood and requires an arterial blood sample. SpO_2 is an indirect, non-invasive estimate of SaO_2 provided by pulse oximetry. While SaO_2 expresses oxygen saturation as the ratio of oxy-haemoglobin to total haemoglobin, SpO_2 considers only the functional haemoglobins.

SpO_2 is defined as the functional oxygen saturation as measured by pulse oximetry, according to (2.2), where $[HbO_2]$, and $[Hb]$ are the concentrations of oxy-, and deoxy-haemoglobin, respectively.

$$SpO_2 = \frac{[HbO_2]}{[HbO_2] + [Hb]} \times 100\% = \frac{[HbO_2]}{[FunctionalHb]} \times 100\% \tag{2.2}$$

Pulse oximetry measures SpO_2 non-invasively and continuously by applying spectroscopic techniques and the Beer-Lambert law (2.3). The Beer-Lambert law describes the transmission of light through a material as a function of incident light intensity (I_0), extinction coefficient (ε), path length of the light (l), and concentration of the substance ($[C]$).

$$I = I_0 e^{-\varepsilon[C]l} \tag{2.3}$$

Fig. 2.2 shows a portion of the electromagnetic radiation extinction spectra for oxygenated and deoxygenated haemoglobin in the near-infrared region. Deoxygenated haemoglobin absorbs more red light (approximately 700 nm), and oxygenated haemoglobin absorbs more infrared light (approximately 900nm). By comparing the optical extinction at the two indicated wavelengths, a pulse oximeter can distinguish between the two haemoglobin species. These wavelengths are selected based on locations in the spectra where there are relatively large extinction coefficient differences between the two haemoglobin species.

A pulse oximeter uses a probe with multiple light emitting diodes (LEDs) with different emission wavelengths and a photodetector. In a conventional probe, two LEDs are used: red (approximately 700 nm) and infrared (approximately 900 nm). These components can be arranged in transmissive or reflective configurations. In the transmissive configuration, the LEDs illuminate a thin perfused tissue, such as a

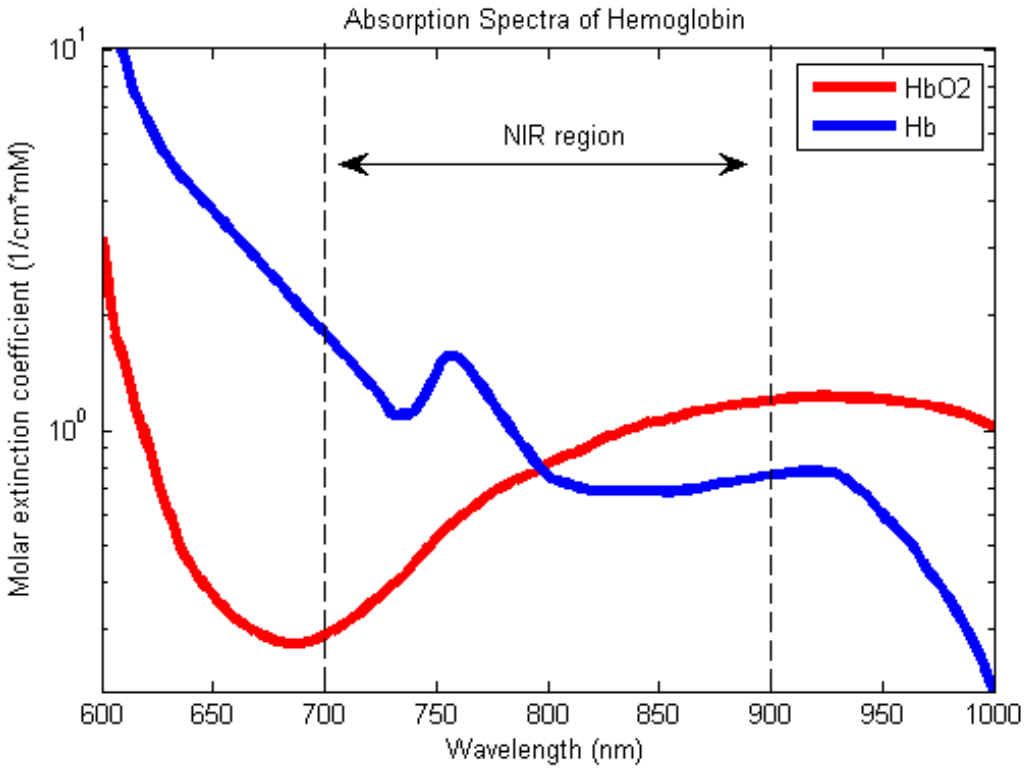

Figure 2.2: Optical extinction spectra of oxygenated haemoglobin (HbO_2) and deoxygenated haemoglobin (Hb) [13].

fingertip or an earlobe, and the photodetector measures the light transmitted to the other side. In the reflective configuration, the LEDs illuminate perfused tissue close to a bone, and the photodetector detects the light reflected from the bone. Fig. 2.3 shows three pulse oximeter probes. The fingertip and earlobe probes are transmissive, and the forehead probe is reflective.

A significant portion of the light extinction between the LEDs and photodetector is due to tissues other than arterial blood. The contribution of each different tissue to the overall light extinction is assumed to be additive. To isolate the effects of arterial blood, the light signal received at the photodetector must be analyzed over a period of time. This light signal is known as a photoplethysmograph (PPG), and is modulated by the pulse pressure signal from the beating heart. During systole, more

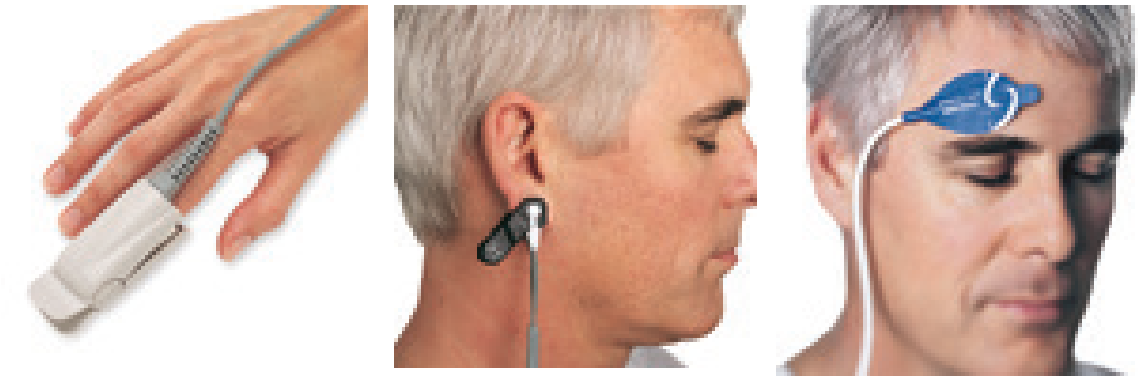

Figure 2.3: Three types of oximeter probes. Fingertip (left) and earlobe (centre) are transmissive, and forehead (right) is reflective. (Images of Nellcor sensors courtesy of Covidien)

blood enters the tissue and light transmission to the photodetector decreases; during diastole blood drains and transmission increases.

The AC component of the PPG signal is assumed to be comprised solely of the pulsating arterial blood, while the DC component is comprised of all of the light absorbing tissues that remain constant. This is demonstrated in Fig. 2.4.

By isolating the AC component of the PPG, the light extinction due to pulsing arterial blood is considered independent of the other tissues between the LED and photodetector. The pulse oximeter normalizes the red and infrared PPGs by their DC components to cancel out the effect of incident light intensity and detector wavelength dependence. To calculate SpO_2, the ratio of amplitudes of the normalized PPGs, known as the "ratio of ratios" or R parameter, is calculated (2.4):

$$R = \frac{AC_{RED}/DC_{RED}}{AC_{IR}/DC_{IR}} \tag{2.4}$$

R is converted to SpO_2 using an empirically derived calibration curve described in Section 2.1.3. A complete derivation of the R parameter and its relationship to SpO_2, starting from the Beer-Lambert model of light absorption, is presented in Appendix A.

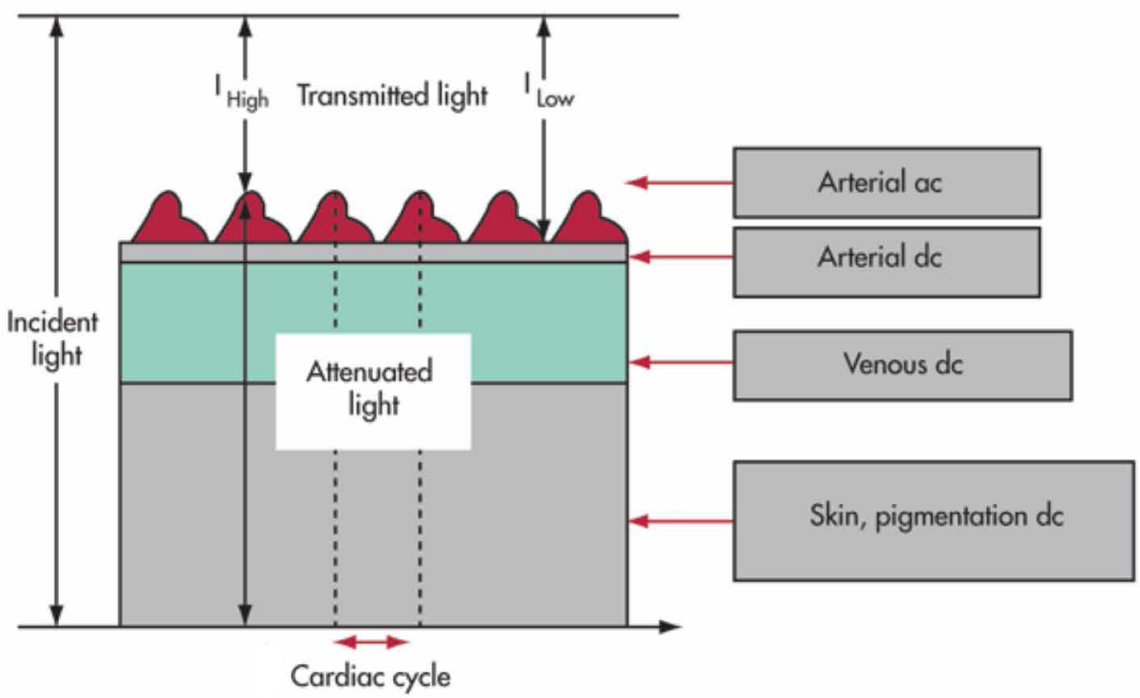

Figure 2.4: Contribution from tissues to light transmission signal. Amplitudes are not to scale. (Adapted from [2])

2.1.3 Calibration

In Appendix A, the analytical relationship between the R parameter and SpO_2 is derived (2.5), where $\varepsilon_{X,\lambda}$ is optical extinction coefficient of molecule X at wavelength λ.

$$SpO_2 = \frac{\varepsilon_{Hb,Red} - \varepsilon_{HbO2,Red}R}{\varepsilon_{Hb,Red} - \varepsilon_{HbO2,Red} + (\varepsilon_{HbO2,Red} + \varepsilon_{Hb,IR})R} \tag{2.5}$$

This calibration function has a number of inherent issues. The extinction coefficients in (2.5) are dependent on the wavelength of the LED. Due to manufacturing tolerances, different instruments may have different peak emission wavelengths and may be subject to drift. Their light emission may also be spread over several wavelengths. Nitzan et al. demonstrated that a wavelength error of only $\pm$ 0.2 nm causes

an error in the distinction coefficient, leading to an error of 0.5 % SpO_2 [14]. Additionally, for any given wavelength, the extinction coefficients of haemoglobin reported in the literature are not in perfect agreement across multiple studies [15].

Further complicating the analytical relationship in (2.5), the Beer-Lambert model does not completely describe the light extinction signal. There are several conditions for validity of the Beer-Lambert law. These conditions stipulate:

- The sample between the light emitter and detector must be homogeneous
- The sample must have zero turbidity (cloudiness caused by solid particles in suspension)
- The rays of incident light must be parallel

Because these conditions are not perfectly met in pulse oximetry, the solution to (2.5) may differ from true SpO_2 values.

To overcome these issues, pulse oximeter calibration curves are derived empirically during the design phase of the device. To derive these curves, clinical trials are set up where healthy volunteers wear pulse oximeters, and the partial pressure of oxygen in the inspired air is reduced temporarily. This induces a short period of hypoxia. R values reported from the oximeter are mapped to SaO_2 values calculated from invasive arterial blood gas analysis. Reasonable accuracy can be obtained using this procedure, but ethical considerations limit calibration below 70% SaO_2. The risk of hypoxic brain damage in the volunteers prevents researchers from inducing low saturation, so reported SpO_2 measurements at low saturations have considerable uncertainty.

2.2 Applications of Pulse Oximetry

2.2.1 Clinical

Pulse oximetry is indicated in any condition where a patient's ability to transport oxygen around the body must be assessed.

Ventilatory support is required when a patient cannot breathe independently. This may be due to general anaesthesia, disease or injury to the lungs and airway. Pulse oximetry is used to assess the performance of mechanical ventilation, and inform the physician if adjustments need to be made to breathing rate, airway pressure, flow volume, or gas mixture [16].

Pulse oximetry is used in the diagnosis of heart and lung disease, as these are the organs responsible for oxygenating and circulating the blood. These conditions can include heart attack, congestive heart failure, anemia, chronic obstructive pulmonary disease (COPD), lung cancer, asthma, or pneumonia [16].

Pulse oximetry may be used in the diagnosis of sleep apnea, a condition characterized by intermittent cessation of breathing during sleep [16]. This may cause a decrease in SpO_2, and the oximeter can measure the severity and duration of hypoxia.

2.2.2 Non-Clinical

There is evidence to suggest that pulse oximetry could be a useful tool for analyzing the training of high performance athletes. Garrido-Chamorro et al. characterized desaturation patterns of athletes while performing maximal oxygen uptake ($\dot{V}O_{2,max}$) tests [17]. The authors hypothesize that establishing these patterns could help evaluate cardiorespiratory adaptation to intense exercise.

Peeling et al. measured oxygen saturation in athletes during high intensity interval work in order to study the effect of oxygen administration during recovery [18]. They

found that administration of hyperoxic gas decreased the time it took for oxygen saturation to return to normal after intense exercise.

Mengelkoch et al. reviewed studies of pulse oximetry during exercise. Oxygen desaturation was often reported during high intensity exercise. This effect was amplified if the athlete was at altitude, or had pre-existing conditions such as asthma [19].

Pulse oximetry is also commonly used by climbers to assess their physiological response to hypoxic conditions at altitude. This is done to manage acclimatization to the hypoxic air and avoid altitude sickness.

2.3 Signal Quality

The ECRI Institute, a research organization promoting evidence-based medicine and patient safety, releases an annual report on health technology hazards to patient safety. In its recent report, the ECRI Institute identified "Inadequate Alarm Configuration Policies and Practices" as the top health technology hazard for 2015 [20]. This includes alarm fatigue, where the false alarm rate is so high that clinicians either waste time responding to them, or ignore them and risk missing true alarms. Next to alarm fatigue, data integrity was identified as the second most significant hazard, whereby missing or incorrect data recorded by medical devices can misinform clinical decisions [20]. Poor signal quality in pulse oximetry is a contributor to both of these hazards.

2.3.1 Artifact Detection in Biological Signals

Because of the significant rate of inadequate alarms cited in the ECRI report [20], there is research interest in implementing smarter alarm policies across a wide range of physiological data. Rather than activating alarms based on a static threshold

in a single biological signal, current research seeks to implement alarms based on individualized trends over a wide variety of signals in order to identify clinically significant events requiring intervention.

Avent and Charlton attribute high false alarm rates to the random nature of biological signals, causing the failure of simple threshold-based alarms [21]. They evaluate research in trend detection and statistical techniques to distinguish between artifacts and clinically significant events.

In her review of false alarms in critical care units, Chambrin recommends careful consideration of what monitors need to be used for an individual patient, as well as careful definition of alarm conditions - including averaging times and clinically significant thresholds. She also recommends a multi-parametric approach with redundant data to improve resilience to artifact [22].

Nizami et al. discuss methodological recommendations for detection of artifacts in biological signals. They recommend a standardized framework for incorporating signal quality assessment into clinical decision making, along with standardized signal quality index (SQI) algorithms for different biological signals [23].

2.3.2 Effects of Motion Artifact in Pulse Oximetry

Investigators have studied the effects of motion artifact on pulse oximetry in clinical settings. Barker and Shah studied the hypoxia alarm rates during motion for a number of instruments, demonstrating false alarms caused by motion artifact [5]. Wiklund et al. noted a 77% false alarm rate in pulse oximetry during post anaesthesia monitoring, caused by sensor displacement, motion artifacts and poor perfusion [24]. In a study in a paediatric intensive care unit, Lawless found 7% of pulse oximeter hypoxia alarms were significant alarms that resulted in altered care [6].

Despite overwhelming evidence that motion artifact causes signal degradation and

false alarms in pulse oximetry, the mechanism is poorly understood. Petterson et al. discuss possible mechanisms by which motion artifact could cause poor signal quality and false alarms [25]. They propose that noise is equal on the red and infrared PPG signals, so as noise increases, R approaches 1 (approximately 85% SpO_2, significantly lower than normal), increasing the likelihood of an hypoxia alarm. They also propose that movement of low-oxygen venous blood could be interpreted by an oximeter as an arterial pulse, further contributing to false hypoxia alarms. The authors admit there is little evidence supporting either of these models.

2.3.3 Signal Quality Assessment in Pulse Oximetry

Researchers have undertaken efforts to develop automatic signal quality assessment on PPG signals. Sukor et al. described a binary signal quality classifier based on morphology of the PPG waveform [26]. In classifying manually annotated "good" and "poor" signals, sensitivity and specificity were reported as 89% and 77% respectively.

Karlen et al.'s SQI algorithm relies on pulse segmentation and cross-correlation of incoming pulses with an ensemble average reference pulse [27]. The pulse segmentation algorithm showed strong performance in identifying and segmenting individual pulses. SQI is compared to manual annotations of signal quality. Success in using the SQI as a binary signal quality classifier is demonstrated, but the authors note that the threshold of this classifier should be application specific.

Li et al. introduced dynamic time warping and a neural network algorithm to develop a waveform morphology based SQI [28]. The authors noted 95% accuracy on the binary classification of manually annotated PPGs.

All of these methods were tested against manual annotations to distinguish between good and poor quality signals. Further study is needed to determine the relationship between the signal quality and SpO_2 measurement error in order to inform

the threshold tuning of a signal quality classifier.

Some SQIs are bolstered by a multimodal approach - Silva et al. used parallel electrocardiogram (ECG) to inform the PPG SQI without relying on waveform morphology [29]. They supported their evaluation by demonstrating the correlation between SQI and signal to noise ratio (SNR) using additive white Gaussian noise.

Many of the published SQIs are evaluated by checking the agreement in heart rate between the PPG signal and a reference ECG. Caution must be used with this approach - accurate heart rate measurement from PPG signals does not imply accurate SpO_2 measurement. In cases where the cardiac pulse is distinguishable in a noisy PPG, the heart rate can be determined even if the PPG amplitudes are altered (affecting SpO_2). Alternatively, if noise is periodic and matches the heart rate, SpO_2 can be affected without the location of the cardiac pulses being obscured.

2.4 Advances in Pulse Oximetry

2.4.1 Calibration-Free Pulse Oximetry

Recent research efforts have attempted to eradicate the dependence of pulse oximeters on empirical calibration. The calibration curves are derived from healthy volunteers over the normal physiological range of SpO_2 values. The resulting curves may not accurately report SpO_2 in critically ill patients outside the normal physiological range.

Reddy et al. discussed a calibration-free method similar to the analytical relationship in (2.5) [30]. Their results demonstrated agreement between their calculations and measured SaO_2 values, but did not address the errors stemming from imprecise peak wavelengths in the LEDs, or the variation of haemoglobin extinction coefficients reported in the literature.

Nitzan et al. further refined the use of the calibration-free method [14]. Laser

diodes were used to improve the precision and accuracy of the emission wavelength in the probe, and SpO_2 calculations were performed using multiple extinction coefficient data sets [15]. Calculated SpO_2 was strongly dependent on which extinction coefficient data set was used.

Both of these studies demonstrate the need for precise determination of the emission spectra of the wavelengths in oximeter probes. Further research is also required to measure the haemoglobin extinction coefficient spectra more precisely. Accurate knowledge of the probe emission wavelengths and haemoglobin extinction coefficients are both prerequisites to the practical adoption of calibration-free pulse oximetry.

2.4.2 Motion Resistant Pulse Oximetry

The sensitivity of pulse oximetry to motion artifact has spurred the development of motion-resistant algorithms. Three dominant technologies are evaluated in the literature: FAST SpO_2 (Fourier Artifact Suppression Technology, Philips Medical Systems), SET (Signal Extraction Technology, Masimo Corp.), and Oxismart (Nellcor) [31].

The Philips Fourier Artifact Suppression Technology (FAST SpO_2) relies on identifying and isolating the PPG signal in the frequency domain. It attempts to find the pulse rate by identifying harmonics and checking the correlation between the red and infrared signals. Narrow filtering of the PPG signals around the pulse frequency reduces the chance that motion artifact bandwidth will overlap with the signal bandwidth [25].

The Masimo Signal Extraction Technology (SET) algorithm takes advantage of the expected relationship between the red and infrared signals (the R value) to inform an adaptive noise filter. For a given segment of PPG signals, adaptive noise filters are generated for the range of R values corresponding to 0% to 100% SpO_2. Applying

these filters to the PPG signals results in the "Discrete Saturation Transform (DST)" - a power spectrum in the SpO_2 domain. The location of the peak of this spectrum corresponds to SpO_2 [8].

The Nellcor Oxismart algorithm takes advantage of the periodicity of the PPG signal to detect individual cardiac pulses. Incoming pulses are compared to an ensemble average of previous pulses to evaluate signal quality. The displayed SpO_2 value is an average of the SpO_2 measurement from several pulses, weighted by their quality [32].

The clinical performance of each of these technologies is evaluated in an array of studies summarized by Giuliano and Higgins in [31]. The authors conclude that while there is no definitive evidence of the superiority of one of these technologies over the others, the motion-resistant technologies are all shown to be improvements over standard pulse oximetry [31].

Chapter 3

Methodology

This chapter provides an overview of the methodology common to the work in this thesis. The research protocol was approved by the Carleton University Research Ethics Board (#100986). Section 3.1 describes the instrumentation system that was used to collect pulse oximetry data. Section 3.2 describes the procedures undertaken to collect a dataset. Section 3.3 describes the method of obtaining SpO_2 measurements from raw PPG signals, and the effect of adjusting the parameters of that calculation. Section 3.4 describes the SpO_2 calculation algorithm used in this thesis.

3.1 System Overview

The data used in this thesis were collected using a standard finger probe (Nellcor DS-100A) and an evaluation module of the Texas Instruments Integrated Analog Front End for Low Cost Pulse Oximeters (AFE4400SPO2EVM), both pictured in Fig. 3.1. The AFE4400 device includes the majority of analog electronics needed in a pulse oximeter in a single integrated chip. A system diagram is shown in Fig. 3.2 [33]. This section details each component of the pulse oximetry system.

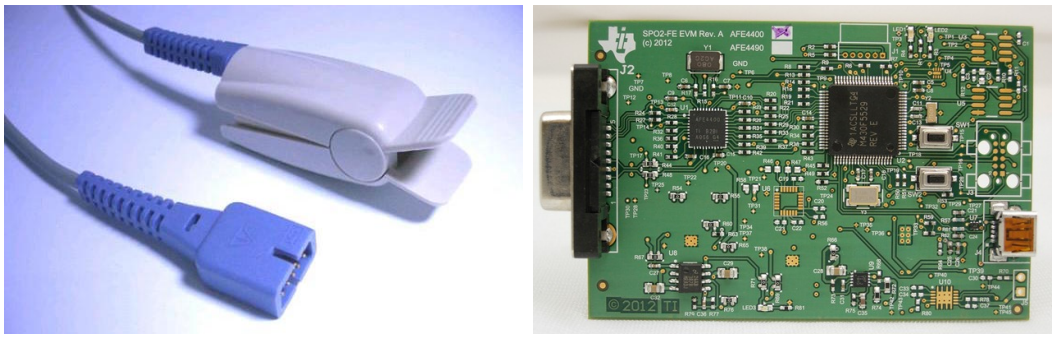

(a) (b)

Figure 3.1: Photographs of a) Nellcor DS-100A pulse oximeter finger probe (courtesy of Covidien) and b) Texas Instruments AFE4400SPO2EVM (courtesy of Texas Instruments).

3.1.1 Receive Section

The features of the PPG signal make data acquisition difficult. According to (2.4), the AC and DC components of the PPG must both be preserved to calculate SpO_2. The DC component of the PPG contributes greater than 99% of the signal amplitude [12]. Amplification of the signal with the purpose of gaining sufficient AC resolution can easily saturate the analog to digital converter (ADC) with the DC signal. As a result, analog signal amplification must be limited to avoid ADC saturation, but this can introduce significant quantization noise in the AC component of the PPG.

The receive circuitry consists of a photodiode in the finger probe, a transimpedance amplifier, and a delta-sigma ADC. The photodiode converts the light signal to a current signal, and the transimpedance amplifier converts current to a voltage signal. The delta-sigma ADC is designed to minimize quantization noise through oversampling. While the maximum expected pulse rate in a PPG is less than 4 Hz, 240 beats per minute (bpm), the photodiode is sampled at 500 Hz. The AFE4400 datasheet claims 13 noise-free bits of resolution in the ADC [33].

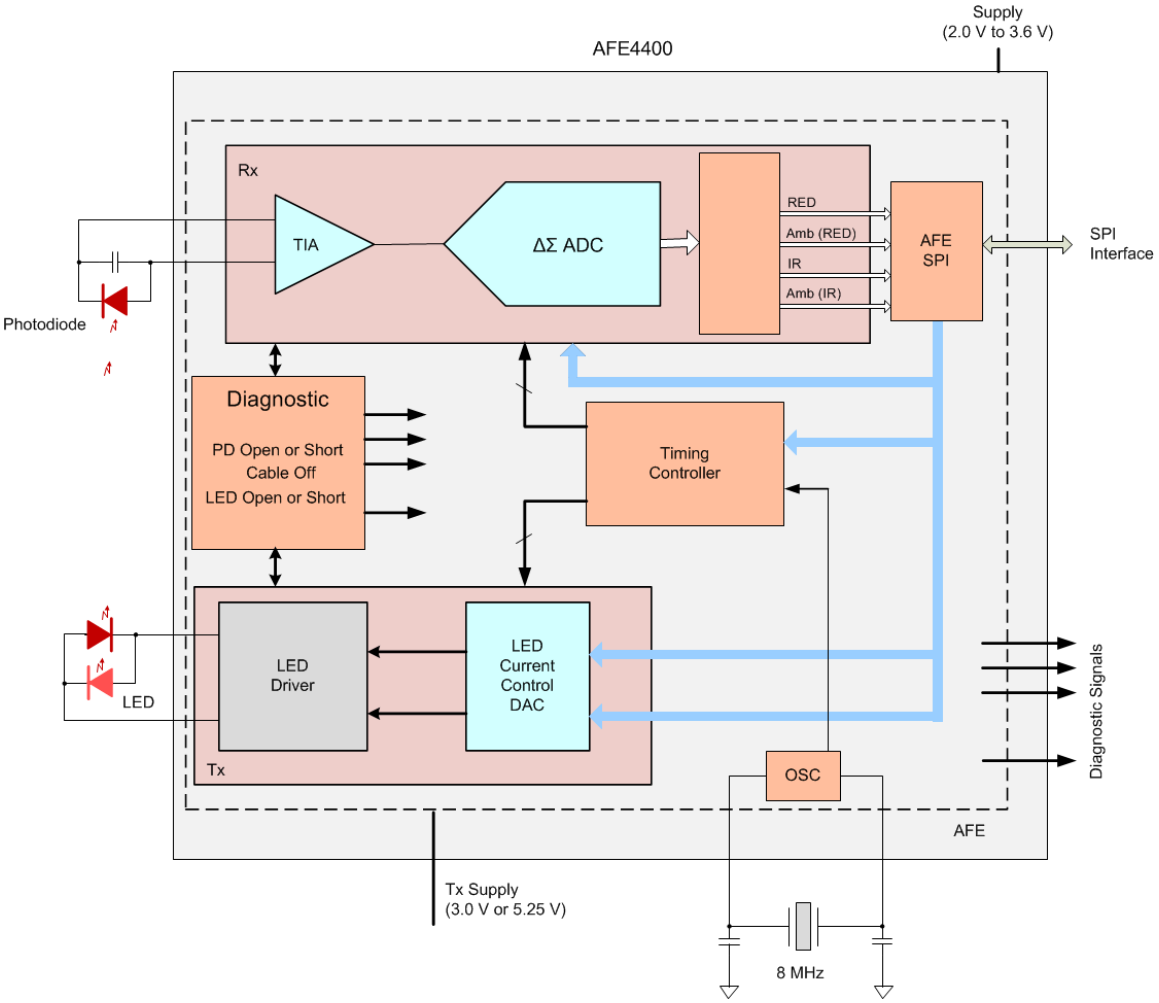

Figure 3.2: System diagram of Texas Instruments AFE4400 [33].

3.1.2 Transmit Section

LED current needs to be carefully controlled to obtain maximum PPG resolution without saturating the ADC. Fig. 3.3 illustrates the ADC range and the upper and lower bounds of the analog signal chain. In order to avoid saturating the transimpedance amplifier, the signal must be kept between -1 and 1 volts.

Increasing the LED intensity increases the AC amplitude of the PPG, but also increases the DC component towards the saturation level of the amplifier. In a process similar to automatic gain control, the LED intensities are independently adjusted by

the LED current control DAC to keep the signals at an ideal level within the ADC range. To prevent saturation while maximizing AC amplitude, Texas Instruments recommends an ideal DC operating point, as is indicated in Fig. 3.3.

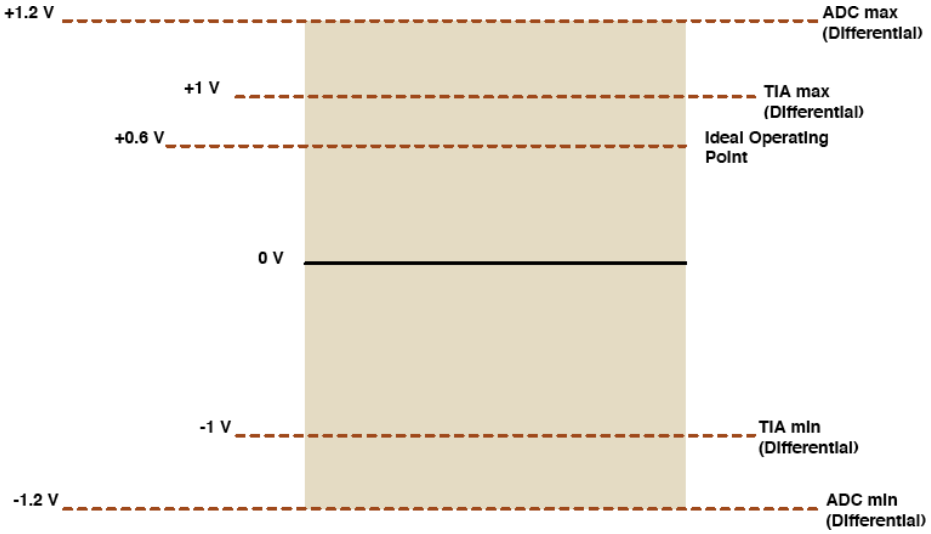

Figure 3.3: Operating range of ADC. Adapted from [33]

3.1.3 Timing Diagram

During each main sampling period, the photodiode is sampled four times: once with the red LED illuminated, once with both LEDs off, once with the infrared LED illuminated, and a final sample with both LEDs off. This sampling sequence results in a red PPG, an ambient light signal associated with the red PPG, an infrared PPG, and an ambient light signal associated with the infrared PPG. This sequence of four samples is performed during the main sampling period of $T = \frac{1}{500}$ seconds, resulting in four parallel 500 Hz signals. Refer to Fig. 3.4 for a timing diagram that illustrates this sequence for two main sample periods.

The resulting output is two PPGs (red and infrared) and two signals representing the ambient light level.

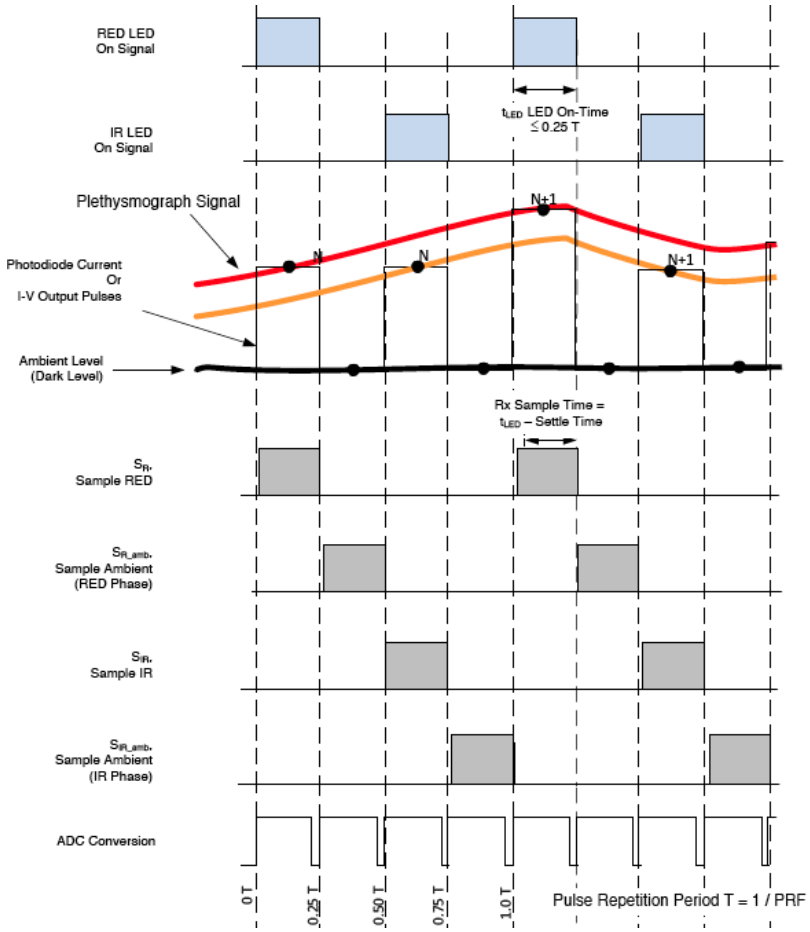

Figure 3.4: Timing diagram for PPG sampling. Adapted from [33]

3.1.4 Probe

The two LEDs and photodiode are housed in a Nellcor DS-100A pulse oximeter finger probe, pictured in Fig. 3.1. The LED wavelengths are specified at 660 ± 5 nm, and 905 ± 5 nm. The probe interfaces with the AFE4400 evaluation module via a standard DB-9 connector.

3.2 Data Collection

Data collection for this thesis was performed using two identical probes and two AFE4400 evaluation modules. Data were collected from 5 healthy subjects, 3 male

and 2 female, aged 26 ± 1 year. Data collection was performed in accordance with a Carleton University Research Ethics Board approved protocol (#100986). Subjects wore a finger probe on the index fingers of their left and right hands. In each of the states described in the following subsections, the left hand remained motionless to function as a control, while the right hand performed the required test condition.

Each tested condition provided eight total signals for each subject:

- Control: red PPG, red ambient, infrared PPG, infrared ambient
- Test: red PPG, red ambient, infrared PPG, infrared ambient

3.2.1 Clean Signal Acquisition

For the first condition, to check the agreement between the two instruments, the subject was instructed to sit calmly and remain motionless for 60 seconds. Care was taken to obtain high quality, contaminant-free signals. The room was darkened to reduce ambient light interference, and the subject rested their hands on the desk to minimize movement. The final signal was truncated to 40 seconds to remove artifacts from the beginning of signal collection.

Due to slight natural variation in the pulse transit times between the hands, perfect pulse to pulse synchronization was not expected between the two instruments. However, the two instruments should agree in their SpO_2 measurements. Differences in the R parameter are attributed to differences in the physical properties of the probes, which would be corrected by calibration in a clinical device.

3.2.2 Contaminated Signal Acquisition

A video was developed in MATLAB (The Mathworks, Natick, MA) to help subjects generate random motion. The subject was instructed to attempt to follow a randomly

moving point on a computer monitor with the test hand, remaining within a 20 cm by 30 cm rectangular window. The movement speed was adjustable to change the severity of the motion. At the highest movement intensity, the hand traversed the window at a maximum rate of approximately 3 Hz. The control hand was covered to eliminate the effects of the moving shadow from the test hand. Again, data collection in each condition occurred for 60 seconds, but the final signals were truncated to 40 seconds to remove artifacts from 'settling in' to the movement. In some cases, subjects inadvertently caused motion artifact in the control hand during testing. Signals were assessed visually for adequate quality, and in these cases of motion artifact on the control hand, the signals were discarded and re-recorded.

The following conditions were generated:

- Low speed motion - 40 seconds
- Medium speed motion - 40 seconds
- High speed motion - 40 seconds

3.2.3 Generating Isolated Noise Signal

The final tested conditions attempted to isolate the motion artifact signal from the PPGs. The subjects wore a sphygmomanometer (blood pressure cuff), shown in Fig. 3.5. The cuff was inflated above the subject's systolic blood pressure, indicated by the loss of pulsations in the PPG signal, shown in Fig. 3.6.

The cuff pressure served to temporarily occlude the brachial artery and prevent a pulse in the finger. Since a normal PPG signal is dependent on the pulse, the signal was eliminated and only noise remained.

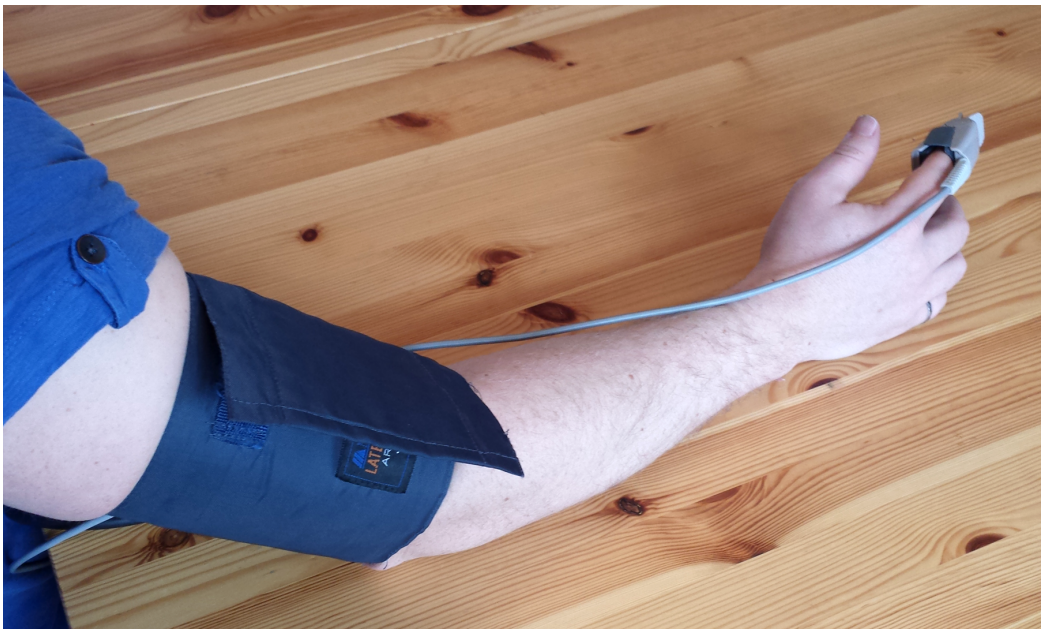

Figure 3.5: Use of sphygmomanometer to attenuate PPG.

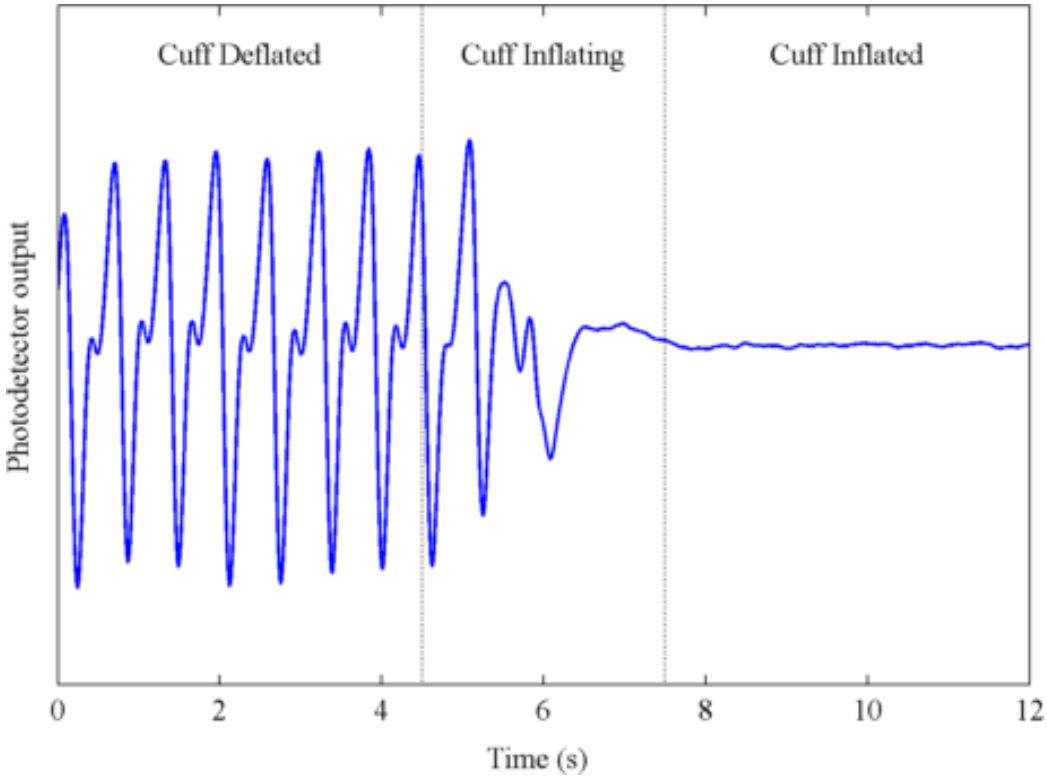

Figure 3.6: Loss of PPG signal indicates sphygmomanometer pressure above systolic blood pressure.

The high motion condition was repeated under this setup. The signal was truncated to the portion where the sphygmomanometer was completely inflated. The signals are 30 seconds long.

There are no strict guidelines on safe blood occlusion time to a limb [34]. However, application of a tourniquet for 1-2 hours to occlude blood flow to a limb is common practice during surgery [35], and most of the literature cautions against exceeding 2 hours of arterial occlusion [34]. Safety precautions for this technique include using the minimum pressure needed to occlude the artery and minimizing time of occlusion. Both of these precautions were observed in this study - the cuff was inflated just above the subject's systolic blood pressure, and only remained inflated for 30 seconds.

3.3 Calculation of R and SpO_2

Despite the straightforward mathematical definition of SpO_2 in Appendix A, the signal processing method chosen to perform this calculation can significantly affect the result. The mathematical definition does not strictly define how AC and DC amplitudes should be calculated, nor is it necessarily robust to quantization or other sources of noise. These issues need to be considered when developing an algorithm to calculate R from raw PPG signals.

Data processing and analysis are performed using MATLAB software. An overview of the data processing steps is presented in Fig. 3.7.

For each condition, the ambient light signals are first subtracted from the PPG signals in an attempt to further mitigate the effects of ambient light. The resulting data are low pass filtered using a fourth order zero-phase Butterworth filter (MATLAB's filtfilt command). The purpose of this filter is to eliminate out-of-band noise,

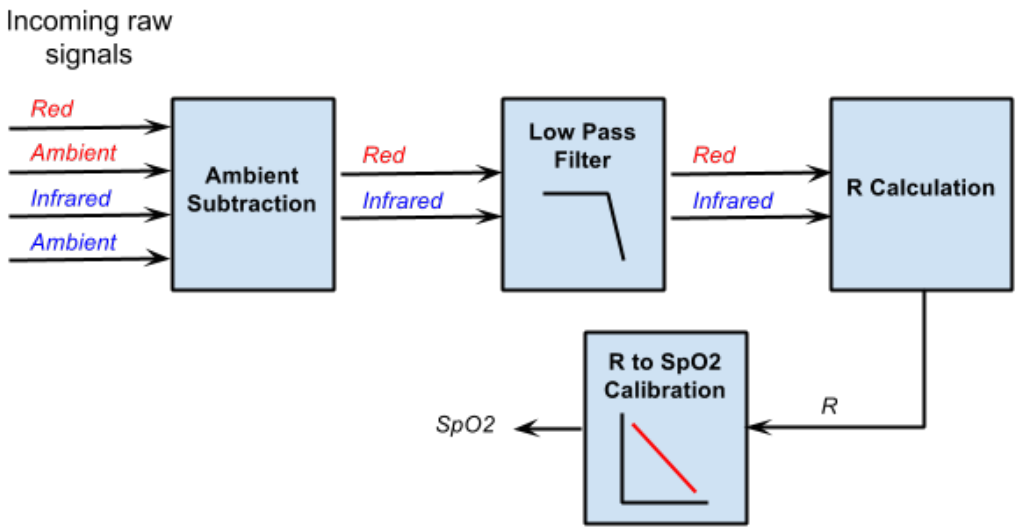

Figure 3.7: Processing of raw PPG signals.

including quantization noise, power line interference and high frequency motion artifact. Ideally, the cutoff frequency can be tuned to eliminate as much information as possible without affecting the SpO_2 measurement.

The AC component of a clean PPG signal from one of the test subjects is shown with its frequency spectrum in Fig. 3.8. Note that the displayed PPG is the raw photodetector output, where low amplitude corresponds to systole and high amplitude corresponds to diastole in the cardiac cycle. A pulse oximeter typically displays this curve inverted, but the current analysis is not affected.

The majority of the AC signal power is found in narrow bands at the cardiac cycle frequency and its harmonics. This subject had a heart rate of about 90 bpm, corresponding to 1.5 Hz. Stuban and Niwayama investigated the effects of the PPG filter bandwidth, and found that the PPG could be low pass filtered just above the cardiac cycle frequency without affecting the SpO_2 measurement [36]. The effect of the low pass filter cutoff frequency is investigated in Section 3.3.2.

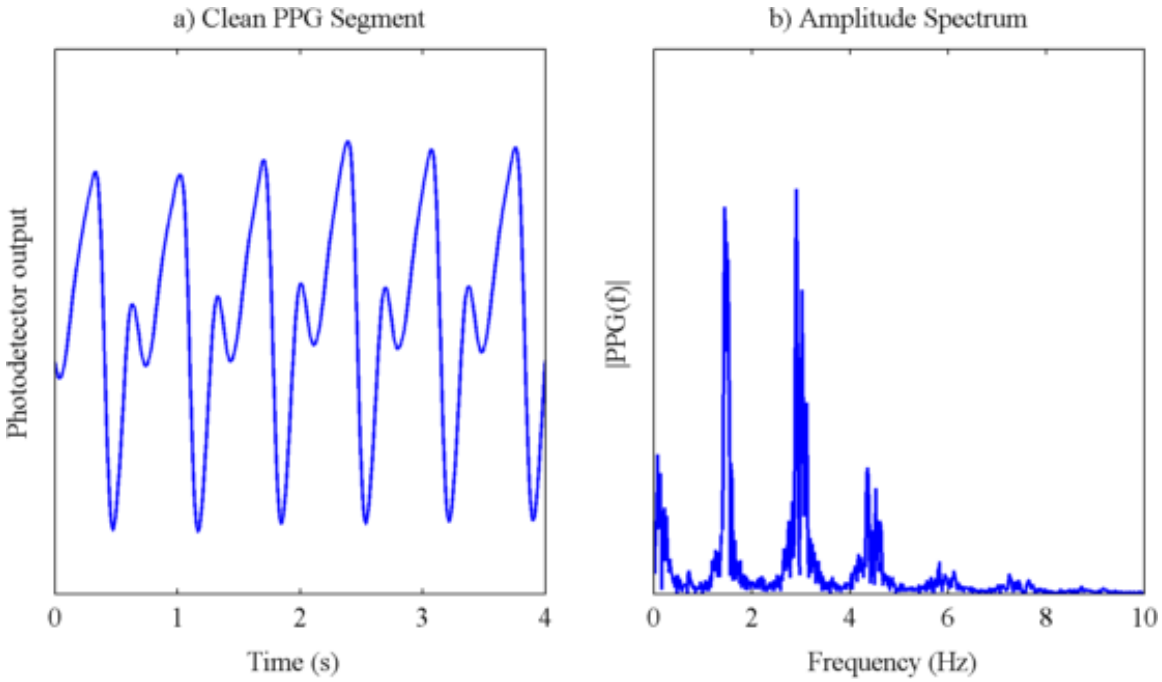

Figure 3.8: A sample PPG signal (AC component only) and its frequency spectrum.

3.3.1 Calibration

The pulse oximetry instrumentation used in these studies was not calibrated. Work in the later chapters analyzes the relative changes in R under testing conditions. Since absolute oxygen saturation values were not needed, absolute calibration was unnecessary.

When R values are being compared between the test and control oximeters, the instrument bias between the two devices is measured in-vivo using high quality contaminant free signals. The test-control bias is also measured for each of the motion conditions, and compared to the instrument bias.

For illustrative purposes, some of the calculated R values in later sections will be expressed as SpO_2 values, derived using the sample calibration curve described in (3.1) and Fig. 3.9. This curve is adapted from [12], and is considered a fairly typical calibration curve for pulse oximeters.

$$SpO_2 = -33R + 118 \tag{3.1}$$

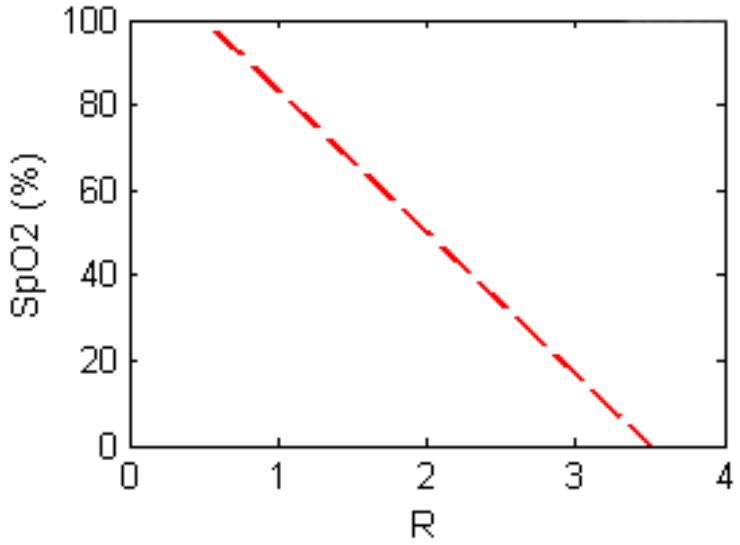

Figure 3.9: Sample pulse oximeter calibration curve. Adapted from [12].

3.3.2 R Calculation Algorithm

Peak-Trough vs. RMS

Two equivalent equations for R calculation are derived in Appendix A and presented in (3.2) and (3.3).

$$R = \frac{ln(I_p/I_t)_{Red}}{ln(I_p/I_t)_{IR}} \tag{3.2}$$

$$R = \frac{AC_{Red}/DC_{Red}}{AC_{IR}/DC_{IR}} \tag{3.3}$$

In (3.2), the peaks and troughs of the PPG waveforms are identified. R is calculated once for each identified peak and corresponding trough. This method has difficulty with motion artifact because of its reliance on successful peak and trough detection. Simple peak detection algorithms cannot distinguish PPG peaks from noise peaks, as demonstrated in Fig. 3.10. A simple peak detection algorithm is successful in identifying pulses in the clean PPG signal, pulse locations are not apparent in the noisy PPG.

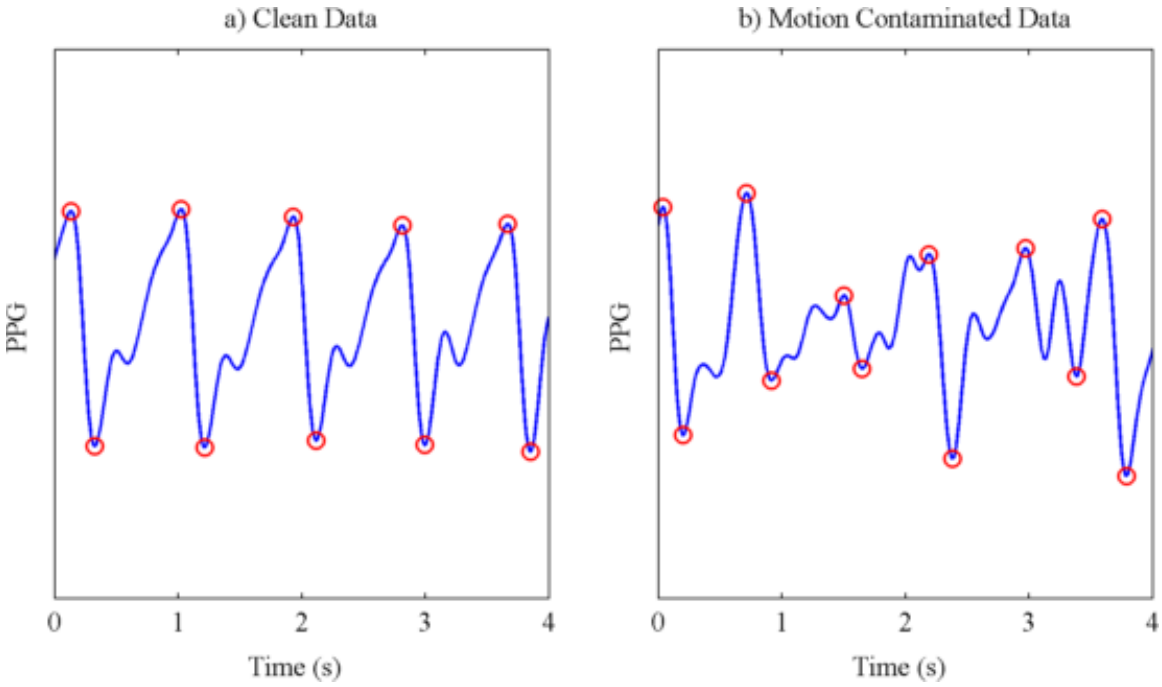

Figure 3.10: Results of basic peak detection algorithm in clean and noisy PPG.

Though (3.2) and (3.3) are mathematically equivalent, (3.3) is a preferable R calculation algorithm because it does not rely on the success of the peak identification algorithm. Rather than calculating amplitude based on only the peak and trough points, every point in a given buffer contributes to the calculation of the RMS amplitude.

Effect of Low Pass Filter Cutoff

Fig. 3.11 illustrates the effect of adjusting the low pass filter cutoff frequency in the preprocessing stage. Sample PPG signals were recorded at an average heart rate of 60 bpm (1 Hz). At each cutoff frequency value, a complete set of calculated SpO_2 values is plotted for a single PPG record. The RMS method was used to calculate R, as described in Section 3.3.2, with a buffer length of one second.

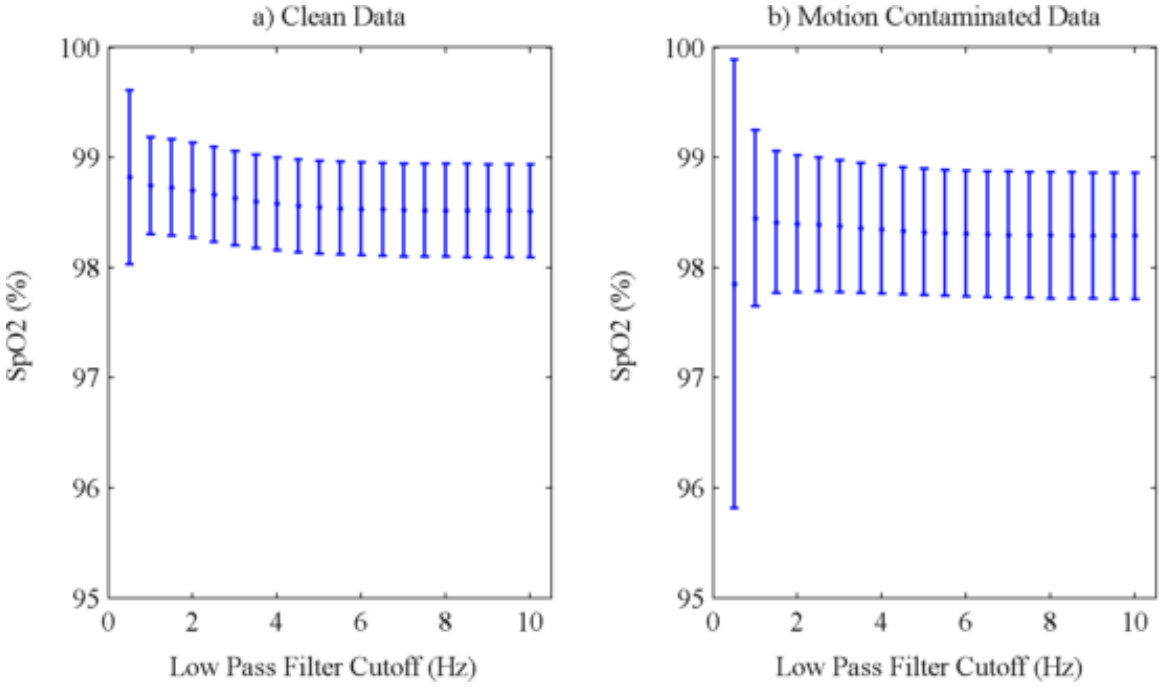

Figure 3.11: Effect of PPG low pass filter cutoff frequency on SpO_2 calculation. SpO_2 values are calculated from the motionless and high-motion data from a single subject. Error bars indicate mean SpO_2 $\pm$ one standard deviation.

Decreasing the low pass filter cutoff has no effect on the clean data until around 1 Hz, and the SpO_2 estimates fall consistently between 98% and 100%. The same trend is observed in the motion contaminated data, yet the SpO_2 readings spread over a greater range. This number is related to the heart rate - below a cutoff frequency of 1 Hz, the 60 bpm PPG signal begins to be attenuated.

Effect of Buffer Length

Fig. 3.12 illustrates the effect of adjusting the buffer in the RMS method of R calculation. Sample PPG signals were recorded at an average heart rate of 60 bpm (1 Hz). At each buffer length value, the PPG signals are split into non-overlapping segments and the SpO_2 is calculated over the entire segment. Increasing the buffer essentially means successive SpO_2 measurements are being averaged over a longer period of time. A short buffer can allow too much signal variation to show on the SpO_2 measurement, but a long buffer can cause the instrument to take longer to respond to drastic changes.

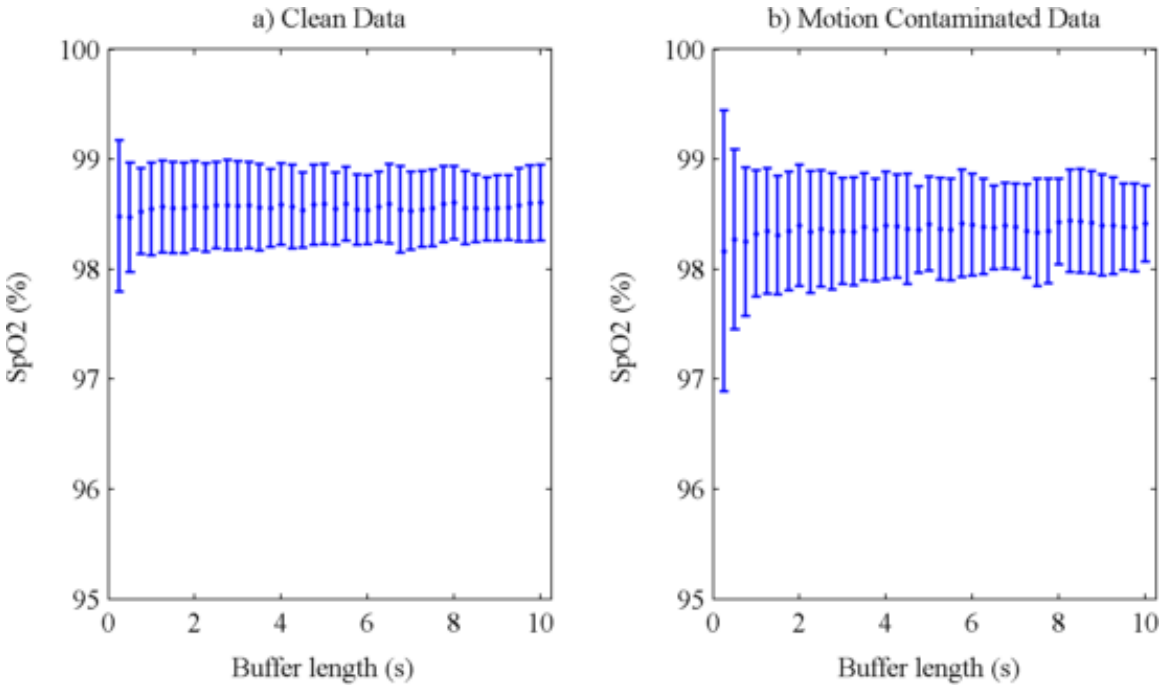

Figure 3.12: Effect of PPG segment length on SpO_2 calculation. Error bars indicate mean SpO_2 $\pm$ one standard deviation.

Decreasing the buffer length has little effect on the clean data until around 1 second, and the SpO_2 estimates fall consistently between 98% and 100%. The motion contaminated data shows considerable variation at the low buffer lengths, but this

variation decreases at a length between 2 and 3 seconds. This number is related to the heart rate - below a buffer length of 1 second, the buffer cannot capture a complete pulse of the the 60 bpm PPG signal.

3.4 Calculation of R and SpO_2 in this Thesis

For the remainder of this document, R is calculated using (3.3). The DC component is defined as the signal amplitude below 0.5 Hz, and the AC component is amplitude above 0.5 Hz. The final R calculation block of Fig. 3.7 is illustrated in Fig. 3.13.

R is calculated using a one-second buffer to minimize the effect of averaging and allow measurements to react quickly to changes in blood oxygen saturation.

The low pass filter in the preprocessing stage is set at 5 Hz to ensure it remains above the maximum cardiac cycle frequency of 200 bpm (3.3 Hz).

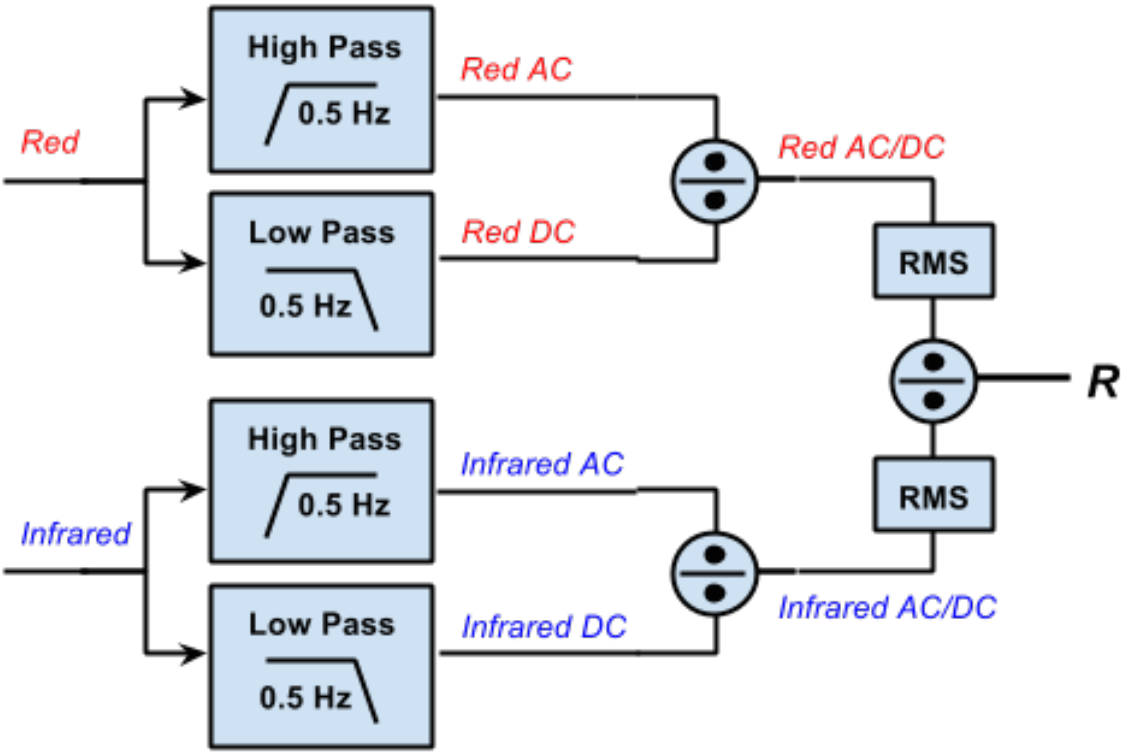

Figure 3.13: System diagram of R calculation algorithm. Inputs are preprocessed red and infrared PPG segments, output is a single R value.

Chapter 4

Evaluating the Effects of Motion Artifact

4.1 Introduction

Previous clinical research suggests that motion artifact may cause a negative measurement bias in pulse oximetry, leading to false hypoxia alarms [5,6,24,25]. However, these studies were performed using commercially available pulse oximeters using proprietary signal processing algorithms. The true extent of measurement errors may be obscured by a variety of signal processing techniques, including averaging, sample and hold, or bias correction algorithms.

The work in this chapter takes a more generic approach to understanding the effects of motion artifact on pulse oximetry readings. The conventional SpO_2 calculation algorithm is evaluated without the aid of error mitigation techniques. Some of the results in this chapter have been disseminated in the author's conference publications [9, 10].

The following sections detail the methodology employed to quantify motion artifact, experimental results with real and artificial data, and discussion.

4.2 Methodology

Using the dataset described in Section 3.2, the methodology described in this section is aimed at observing the statistical parameters of R measurements. The parameters of the motion contaminated data were compared to those of the clean data. A dataset of artificially contaminated PPGs is generated to examine the relationship between the R measurements and signal to noise ratio (SNR).

4.2.1 Real Contaminated Data

Each PPG signal is processed as described in Section 3.4, including calculation of R and calibration. Since the R calculation occurs in one-second buffers and the signals are 40 seconds long, 40 unique R measurements were calculated for each hand, over each test condition. The sample calibration curve in Section 3.3.1 was applied to convert R to SpO_2.

The SpO_2 values from the control signals were subtracted from the test signals to produce an array of biases for each test condition. These values were used to calculate the instrument bias in the motionless condition, and compare that to biases observed in each of the movement conditions:

- **Instrument Bias**: The difference between the test and control SpO_2 values for the motionless condition.
- **Measurement Bias**: The difference between test and control SpO_2 values for each of the movement conditions.

Measurement Bias

For each subject, two-tailed Welch's t-tests were performed to check if the mean SpO_2 biases in movement conditions were significantly different from the instrument

bias. Welch's t-test allows for comparison of samples of unequal variance. The null hypothesis (H_0) for any given condition states that the mean of the biases between the test and control SpO_2 values is equal to the instrument bias. Rejecting H_0 implies a measurement bias in SpO_2 for the given condition.

H_0 can be rejected at a significance level of $\alpha = 0.05$, but since 15 tests were performed (3 for each of the 5 subjects), a Bonferroni correction was applied to reduce the chance of Type I error. The adjusted significance level is $\alpha = 0.003$.

Measurement Variance

For each subject, a right-tailed Chi-square test of variance was performed to check if the variance of SpO_2 bias in the movement conditions was greater than that of the motionless condition. The null hypothesis (H_0) for any given condition states that the SpO_2 variance in the movement conditions is less than or equal to the SpO_2 variance in the motionless condition.

H_0 can be rejected at a significance level of $\alpha = 0.05$, but since 15 tests were performed (3 for each of the 5 subjects), a Bonferroni correction was applied to reduce the chance of Type I error. The adjusted significance level is $\alpha = 0.003$.

If (4.1) is satisfied, the given movement condition has significantly more measurement variance than the motionless condition (H_0 is rejected). In (4.1), N is equal to the number of SpO_2 measurements in each condition, s is the standard deviation of the movement condition under test, and s_0 is the standard deviation of the motionless condition.

$$(N-1)(s/s_0)^2 > \chi^2_{1-\alpha,N-1} \tag{4.1}$$

4.2.2 Artificially Contaminated Data

In order to gain tighter control of the SNR, a set of artificially contaminated signals were generated. After DC normalization, the AC portion of the isolated noise signals (described in Section 3.2.3) were added to the AC portion of clean PPG segments. For each one-second buffer segment, R and SNR were calculated according to (4.2) and (4.3).

$$R = \frac{AC_{Red}/DC_{Red} + k(AC_{Red,noise}/DC_{Red,noise})}{AC_{IR}/DC_{IR} + k(AC_{IR,noise}/DC_{IR,noise})} \tag{4.2}$$

$$SNR = 20log_{10}\left(\frac{AC_{IR}/DC_{IR}}{k * (AC_{IRnoise}/DC_{IRnoise})}\right) \tag{4.3}$$

Note that the PPG and noise are DC-normalized before they are scaled and added. This operation is valid because a real contaminated signal would not include DC components for both the noise and the PPG; the DC component depends on the brightness of the LEDs and ambient light.

The scaling factor k was adjusted to cover SNRs ranging from -30 to 40 dB, and the relationship between SNR and SpO_2 is plotted for each subject.

4.3 Results

4.3.1 Real Contaminated Data

Sample PPGs for each of the motion conditions are displayed in Fig. 4.1, after AC isolation, normalization and low pass filtering. The effect of noise is visually evident. While PPG pulses are still discernible in the movement conditions, they are obscured compared to the motionless condition.

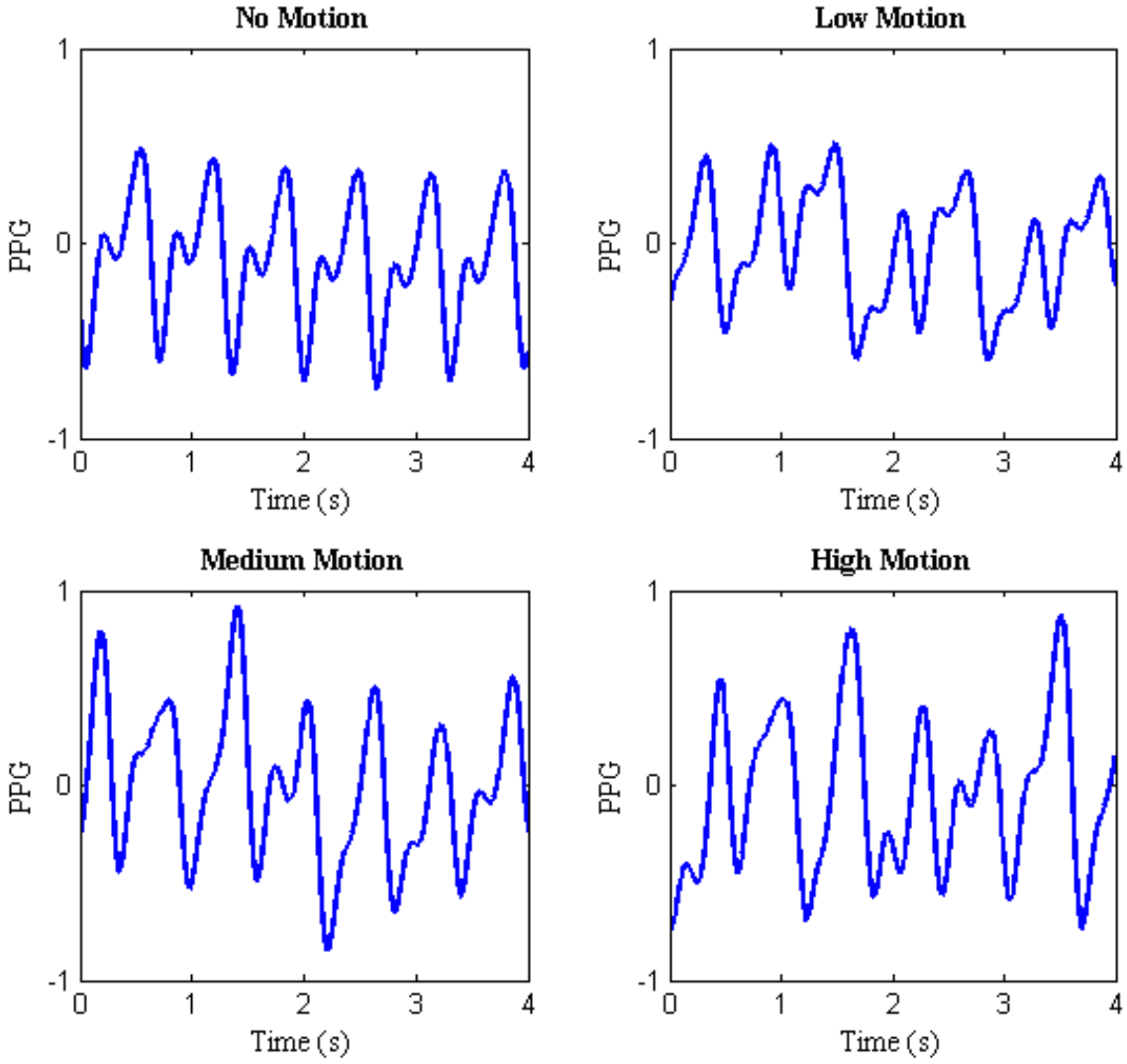

Figure 4.1: Sample PPGs for each of the movement conditions tested.

Table 4.1 presents a summary of the test-control SpO_2 biases. Mean and standard deviation of the differences are reported for each movement condition for each subject.

Assuming that the SpO_2 biases between test and control data fell on a Gaussian distribution, MATLAB's "mle" function was used to calculate the maximum likelihood estimate of mean and standard deviation. Probability distribution functions

Table 4.1: SpO_2 bias between test and control data.

Subject	No Motion		Low		Medium		High	
	$\bar{x}$	s	$\bar{x}$	s	$\bar{x}$	s	$\bar{x}$	s
1	-0.9976	0.1917	-1.4348	0.6975	-1.7651	0.7719	-1.7129	0.8711
2	-0.5489	0.3009	-0.8690	0.6630	-0.3507	0.4299	0.0260	1.1067
3	-0.7264	0.2561	-1.6403	0.9297	-0.7152	1.0011	-1.7531	1.6284
4	-1.8228	0.4924	-1.6077	0.8395	-0.9453	0.9176	-2.6013	1.5033
5	-1.8414	0.5723	-0.3453	0.6571	-1.1321	0.8173	-2.3340	1.2570

based on these parameters were generated. Fig. 4.2 is a plot of the probability distribution functions for one of the subjects, comparing the test-control measurement bias for the motionless and all three movement conditions. The remainder of the subjects' plots are shown in Fig. 4.3.

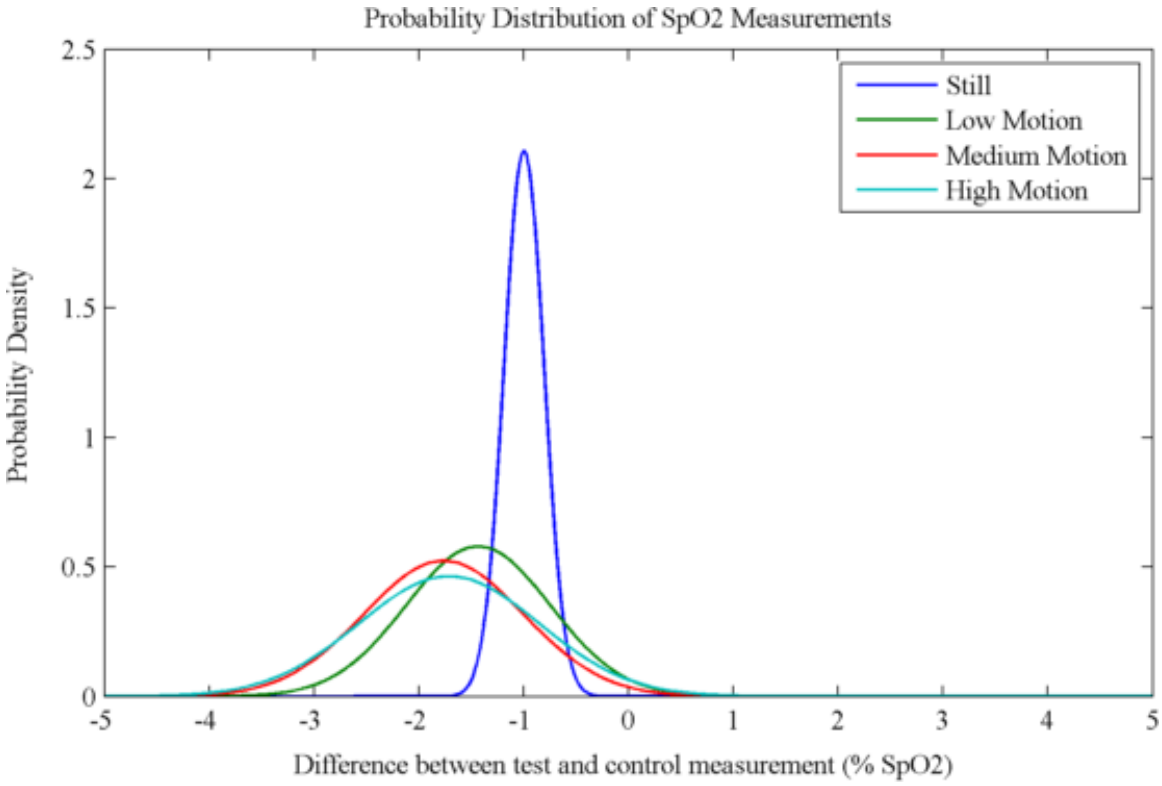

Figure 4.2: Probability distributions of SpO_2 biases: Subject 1.

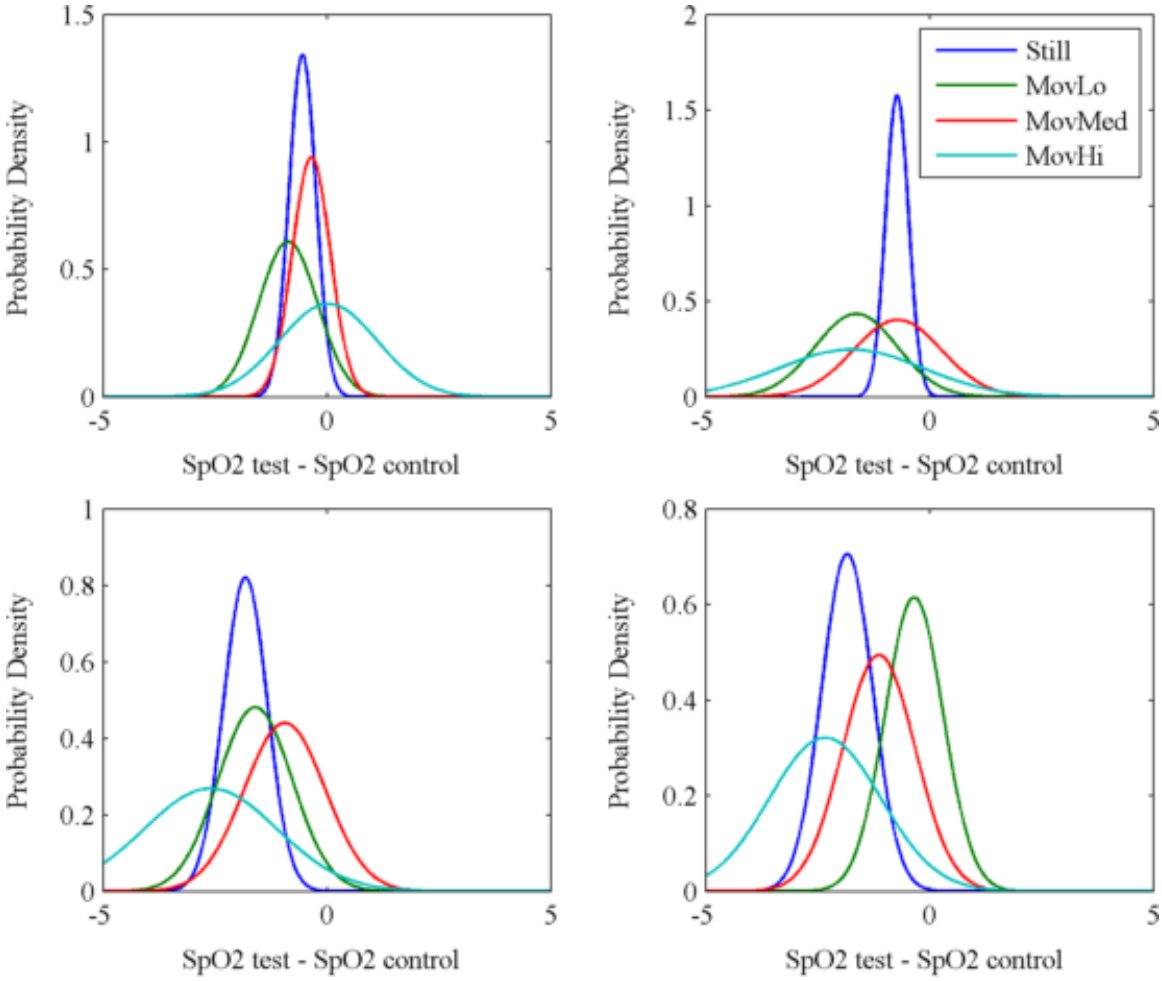

Figure 4.3: Probability distributions of SpO_2 biases: Subjects 2-5.

The dark blue lines show the test-control SpO_2 bias in the motionless condition, indicating instrument bias. A negative instrument bias is apparent in each of the subject's plots. The same instruments were used for test and control for each subject, so similar instrument biases are expected. The other three distributions represent the measurement biases in the three tested motion conditions. Fig. 4.2 indicates the measurement bias for all three movement conditions is different than the instrument bias, indicating that the bias is caused by motion artifact. Tests are performed for difference in bias and standard deviation of SpO_2 measurements between motion and motionless conditions in each subject.

Measurement Bias

Table 4.2 presents the results of Welch's t-test, comparing the test-control bias in each movement condition to the bias in the motionless condition. A positive t-test implies there was SpO_2 measurement bias in the given condition that was not explained by instrument bias.

Table 4.2: Test for SpO_2 Bias During Motion.

Subject	Low Motion	Medium Motion	High Motion
1	$p = 0.0004$	$p < 0.0001$	$p < 0.0001$
2	$p = 0.0074$	$p = 0.0196$	$p = 0.0027$
3	$p < 0.0001$	$p = 0.9454$	$p = 0.0003$
4	$p = 0.1671$	$p < 0.0001$	$p = 0.0031$
5	$p < 0.0001$	$p < 0.0001$	$p = 0.0281$

Shaded cells indicate statistical significance.

Statistically significant bias was found in 9 of the 15 motion conditions measured. This test only determined the presence of a bias, not its direction; in fact, positive and negative biases were both observed.

Biases were pooled across subjects and are presented in Fig. 4.4. The plot shows $\bar{x} \pm s$ of all subjects' SpO_2 biases. None of the movement conditions show a measurement bias significantly different from the instrument bias.

Measurement Variance

Table 4.3 presents the results of the Chi-square test for variance. A positive test implies there was an increase in SpO_2 measurement variance in the given condition over the natural instrument variance. Statistically significant increases in variance

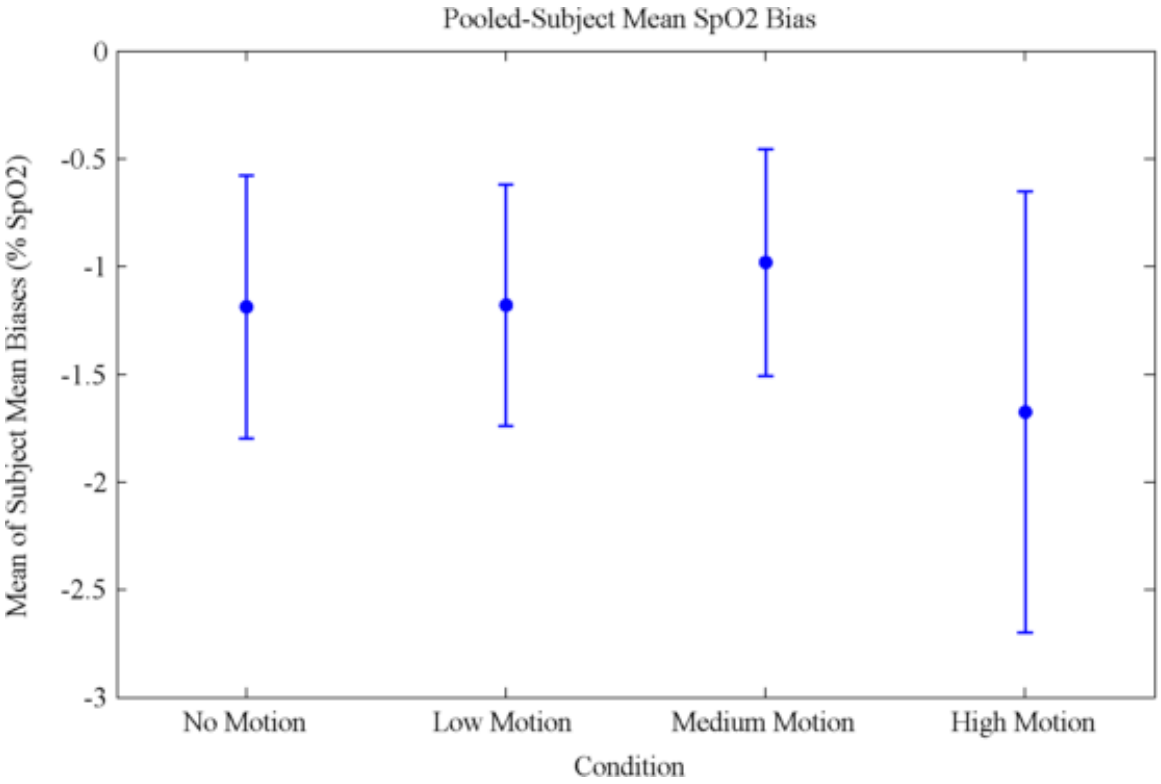

Figure 4.4: Mean SpO_2 bias across subjects. Error bars represent standard deviation of the subject means.

Table 4.3: Test for SpO_2 Variance Increase During Motion

Subject	Low Motion	Medium Motion	High Motion
1	$p < 0.0001$	$p < 0.0001$	$p < 0.0001$
2	$p = 0.9805$	$p = 0.0643$	$p = 0.0009$
3	$p < 0.0001$	$p < 0.0001$	$p < 0.0001$
4	$p < 0.0001$	$p < 0.0001$	$p < 0.0001$
5	$p = 0.2383$	$p < 0.0007$	$p < 0.0001$

Shaded cells indicate statistical significance.

were found in 12 of the 15 motion conditions measured.

SpO_2 standard deviations were pooled across subjects and are presented in Fig. 4.5. The plot shows $\bar{x} \pm s$ of all subjects' SpO_2 standard deviations. All of

the movement conditions show greater standard deviation than the motionless condition. The low and medium motion standard deviations are indistinguishable, but the high motion standard deviation is significantly greater than low and medium motion.

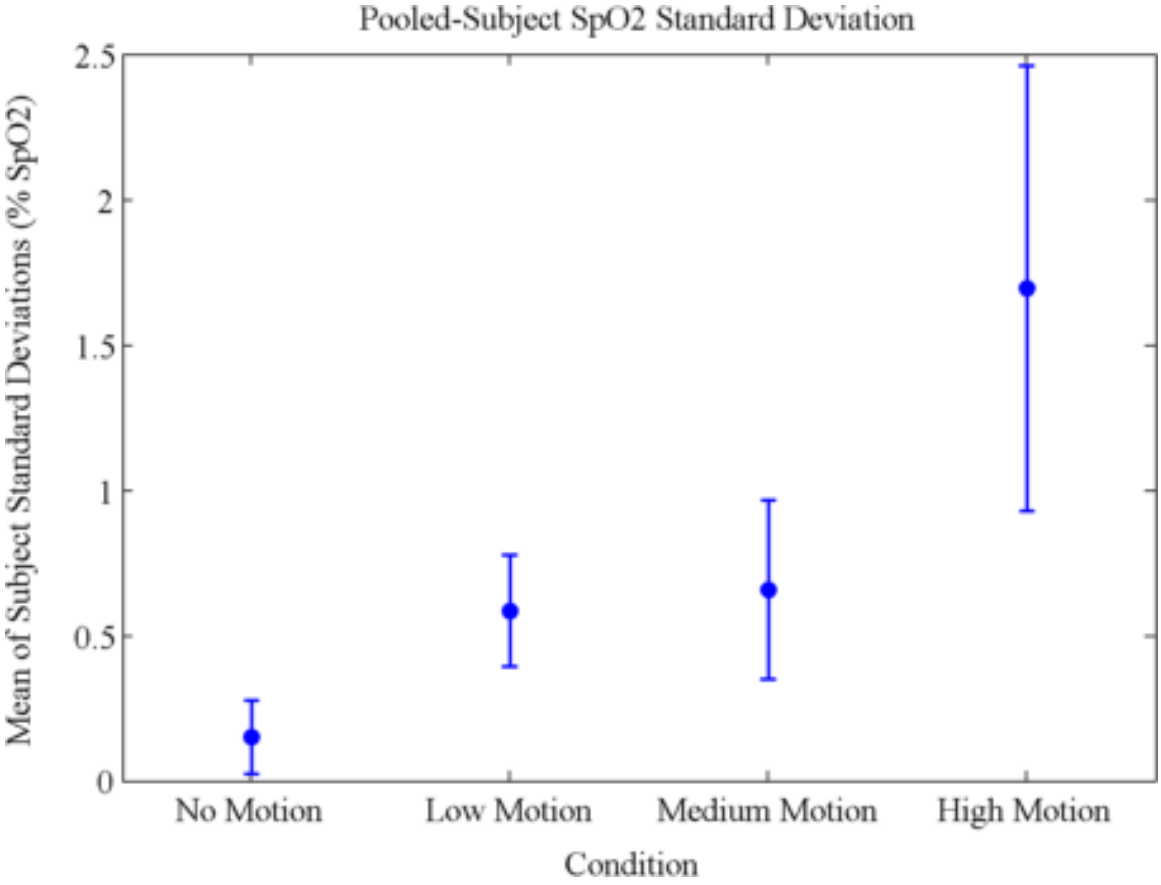

Figure 4.5: Mean SpO_2 standard deviation across subjects. Error bars represent standard deviation of all subjects SpO_2 standard deviations.

4.3.2 Artificially Contaminated Data

Using the artificially contaminated data described in Section 4.2.2, SpO_2/SNR scatterplots were generated for each subject with SNR ranging from -30 to 40 dB. Each point represents the SpO_2 and SNR for a single one-second PPG segment, as defined by (4.2) and (4.3). Fig. 4.6 is a scatterplot for one of the subjects. The red lines

indicate the mean SpO_2 ± one standard deviation of the motionless data, for comparison. The remainder of the subjects' plots are shown in Fig. 4.7. The artificially contaminated data shows relationships between SpO_2 bias and SNR, and SpO_2 variance and SNR. The bias and variance both begin to increase at SNRs below 20 dB in all subjects. Some of the SpO_2 values at low SNR are greater than 100% - these erroneous values would be truncated by a pulse oximeter.

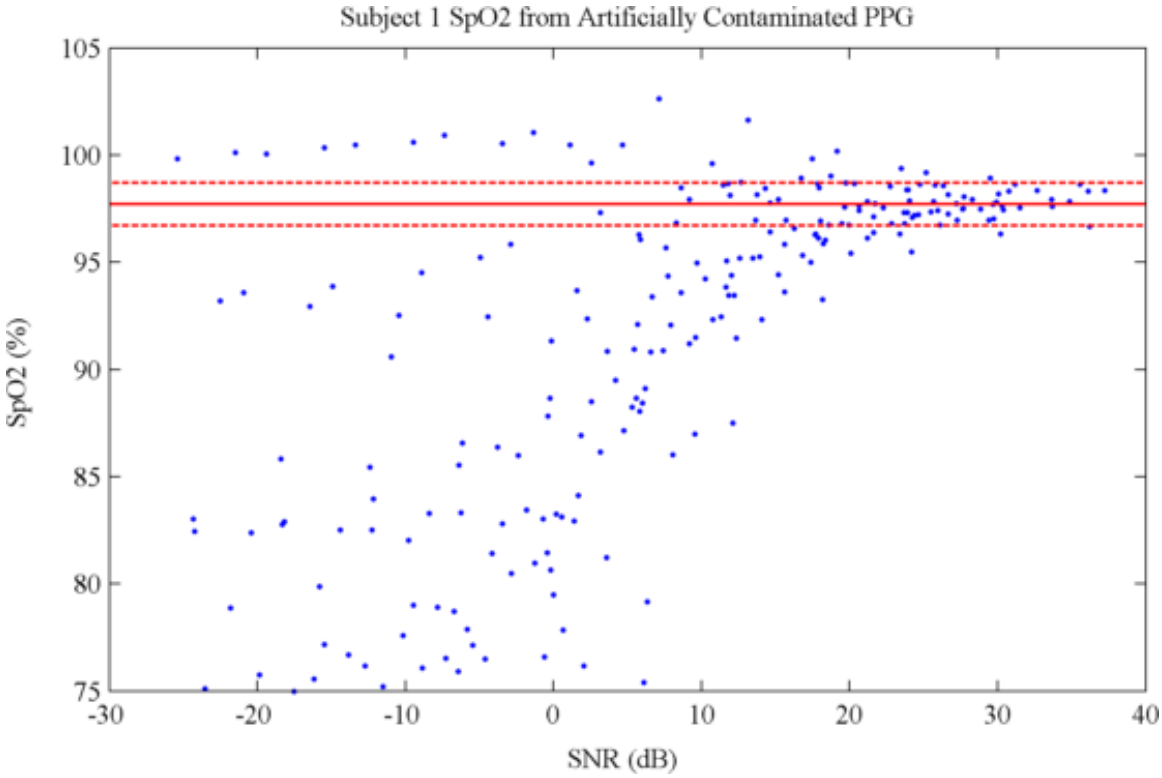

Figure 4.6: Relationship between SpO_2 and SNR in artificially contaminated signals: Subject 1. Each point represents the SpO_2 and SNR of a single one-second segment of PPG data, calculated according to (4.2) and (4.3). Red lines indicate mean ± one standard deviation of SpO_2 values in the clean signal.

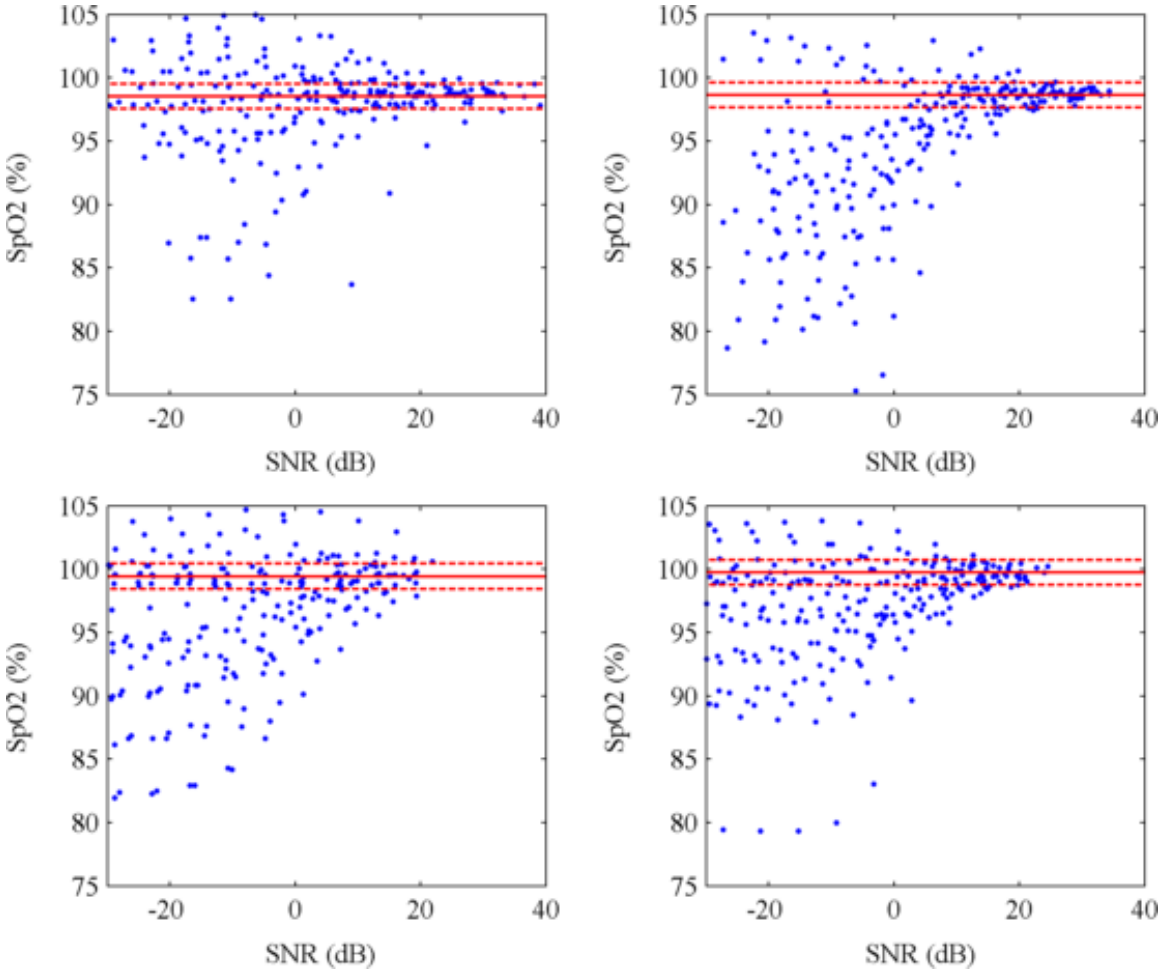

Figure 4.7: Relationship between SpO_2 and SNR in artificially contaminated signals: Subjects 2-5. Each point represents the SpO_2 and SNR of a single one-second segment of PPG data, calculated according to (4.2) and (4.3). Red lines indicate mean $\pm$ one standard deviation of SpO_2 values in the clean signal.

4.4 Discussion

4.4.1 Measurement Bias

The results from the real data showed little evidence of a systematic negative measurement bias in SpO_2 during motion. While the results did demonstrate biases that were significantly different from the instrument bias in some tests, observation of

the plots in Fig. 4.2 and Fig. 4.3 show that the biases could be positive or negative. Furthermore, when the subjects were pooled, Fig. 4.4 showed that there was no significant bias beyond the instrument bias across subjects.

While some motion-induced biases were shown, care must be taken to distinguish statistical significance and clinical significance. The greatest measurement bias related to motion artifact observed in Table 4.1 was 1.5 % SpO_2. Since the normal physiological range of SpO_2 is $> 95\%$, a bias of 1.5% in a healthy person may carry little clinical significance. However, this bias becomes clinically significant for SpO_2 measurements near the hypoxia alarm threshold, and could cause false alarms or missed alarms.

The results from the artificially contaminated data, by observation of the plots in Fig. 4.6 and Fig. 4.7 demonstrated a clear negative SpO_2 measurement bias at low SNRs. Two possible conclusions can be drawn from this observation:

1. The artificial contamination model is a poor reflection of real world results, or
2. The real data did not simulate sufficiently low SNRs to observe measurement bias

The artificial contamination model predicted measurement biases of the same scale as those reported in previous literature [5, 6, 8, 25]. It is likely that the real data collected in this study did not simulate sufficiently low SNRs to demonstrate similar results.

This observation reflects a common issue in motion artifact studies - it is difficult to characterize, quantify and reproduce clinically significant motion artifact. In their meta-analysis of studies on motion tolerant pulse oximeters, Giuliano et al. note a variety of different methodologies for simulating motion artifact, including passive (machine generated) and active (patient generated) [31]. In reality, motion artifact

experienced in clinical settings can stem from a variety of sources, including walking, falling, having a seizure, or rolling over in bed. These different types of motions may have different effects on pulse oximetry measurements, and can be difficult to reproduce in a controlled study.

4.4.2 Measurement Variance

The results from both the real data and the artificially contaminated data showed an increase in measurement variance during movement. Even using the conservative Bonferroni correction to test statistical significance, 12 out of 15 tests on the real data rejected the null hypothesis. When the variances were pooled across subjects, Fig. 4.5 shows that all three motion conditions had increased variance over the motionless condition. While the low and medium levels had indistinguishable variances, the high motion condition had greater variance than low and medium motion.

The results from the artificially contaminated data, by observation of the plots in Fig. 4.6 and Fig. 4.7 demonstrated an increased SpO_2 measurement variance at low SNRs, especially below a threshold of approximately 15-20 dB. This finding supports the finding of increased variance in the real data.

In a clinical setting, an increase in variance may be sufficient to cause hypoxia alarms without the presence of a systematic measurement bias. This would happen if a pulse oximeter ignored measurements above 100% SpO_2, truncating the upper tail of the normal distribution while keeping the lower values.

4.5 Chapter Summary

The real data showed an increase in variance of SpO_2 measurements during motion. This finding was corroborated by the artificially contaminated data - measurement

variance was shown to increase as signal quality decreased.

The real data showed evidence that measurement bias is possible during motion artifact, but there was no strong evidence for the systematic negative bias predicted in previous literature [5, 6, 8, 25]. The difficulty in controlling the level of a subject's motion may have contributed to this effect. It is possible that the movement conditions tested did not cause sufficient signal degradation, and as a result the predicted effects were not observed.

The artificially contaminated data clearly showed a negative measurement bias at low signal to noise ratios. This finding is consistent with results reported in previous literature using real signals [5, 6, 8, 25].

An increase in measurement variance could likely be mitigated by increasing the size of the SpO_2 calculation buffer, or implementing a rolling average of several SpO_2 calculations. However, these techniques would lead to a system that is less responsive to sudden changes in SpO_2. The trade-off between measurement accuracy and responsiveness could be tuneable in a real system, and this threshold would likely be application specific.

Further research is indicated in characterizing and quantifying clinically significant motion artifact, and replicating this motion in a controlled environment. This will allow better comparison between the real and artificially contaminated data.

Further research is also indicated in assessing the susceptibility of different types of pulse oximeter probes to motion artifact. For example, reflective probes may show similar or worse susceptibility to motion artifact as the transmissive probes used in this study. However, reflective probes can record signals on parts of the body that move less relative to the hands, such as the sternum or forehead.

Chapter 5

Analytical Models of SpO_2 Error

5.1 Introduction

As discussed in Section 2.3, the vulnerability of pulse oximetry to motion artifact is well documented [5, 6, 24, 25]. Motion artifact was shown to cause false hypoxia alarms, typically defined as $SpO_2 < 90\%$. This indicates that motion artifact may cause a negative bias in SpO_2 measurements, or may cause sufficient variance in SpO_2 measurements to produce values below the alarm threshold.

Two predominant explanations for a motion-induced measurement bias have been proposed in the literature, but few experimental investigations have been done to determine the extent to which they are valid [8, 25]. The first model assumes that the noise is approximately equal on the red and infrared signals. Therefore, as noise increases, the R ratio is dominated by $Noise/Noise$ and approaches 1, corresponding to SpO_2 of approximately 85%. The second model assumes that movement causes low-oxygen venous blood to become pulsatile, making the device unable to distinguish between arterial and venous blood.

This chapter seeks to:

- Formally define the relevant assumptions and develop a mathematical definition

of each model

- Calculate the effects of these assumptions on the R measurement
- Discuss the agreement between the analytical models and experimental observations

The following sections include a description of the proposed models, an analysis of the isolated motion artifact signals, and a discussion of the relationship between the analytical models and experimental data.

5.2 Proposed Models

In an ideal noise-free signal, the absorption of light is modulated by path length changes through the arterial blood due to the cardiac pulse. The models described in this section introduce a possible motion related signal modulation, state the relevant assumptions, and calculate the predicted effect of motion on the R values.

In these models, the measured R value is assumed to be a non-linear combination of R_S and R_N. R_S is the ratio of red and infrared PPG signal amplitudes, and R_N is the ratio of the red and infrared noise amplitudes. For high SNR, $R \rightarrow R_S$, and for low SNR, $R \rightarrow R_N$.

5.2.1 Varying Path Length

This model assumes motion artifact noise is due to relative motion between the tissue and the oximeter probe. This causes variation of the path length between the light detector and emitters, illustrated in Fig. 5.1.

In modelling the light absorption in the oximeter probe, the Beer-Lambert equation is split into additive components for light absorption due to Hb, HbO_2, and other

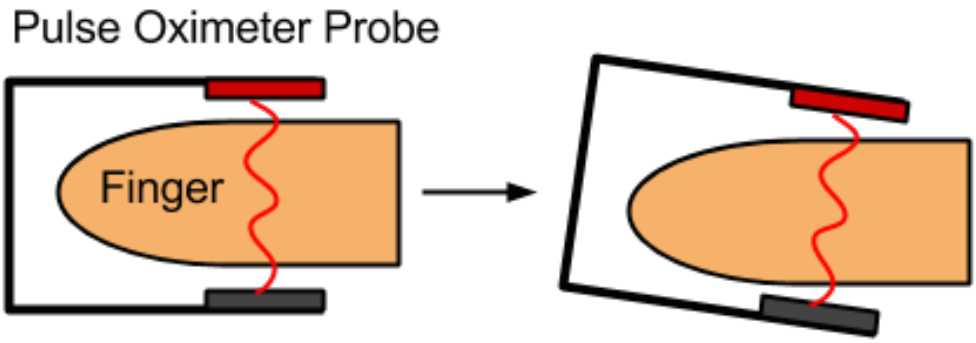

Figure 5.1: Illustration of relative motion between the pulse oximeter probe and the finger.

tissues (A.3). This is done to take advantage of the path length modulation of the arterial blood pulsation. Arterial blood pulsation is not included in the pure noise (R_N) equation. Consequently, the Beer-Lambert equation can be expressed as a function of catch-all terms (5.1), where ε_λ encompasses the wavelength-dependent optical extinction coefficients of all of the tissues in the measurement site, $[C]$ encompasses tissue concentrations, and l is the path length of the red or infrared light.

$$I_t = I_0 e^{-\varepsilon_\lambda [C] l} \tag{5.1}$$

Similar to the derivation in Appendix A, a Δl term is introduced (5.2). In this case, it refers to the change in path length related to the probe shift, rather than the cardiac cycle. Since the red and infrared LEDs are not in the exact same locations, the change in path length may not be exactly the same for each LED. Therefore, Δl is wavelength dependent (Δl_λ).

$$I_p = I_0 e^{-\varepsilon_\lambda [C] (l + \Delta l_\lambda)} \tag{5.2}$$

The rest of the R_N derivation proceeds as it does in Appendix A: calculating

$ln(I_p/I_t)$ removes the exponential function and the dependence on I_0 and l (5.3).

$$ln(I_p/I_t)_\lambda = ln\left(\frac{I_0 e^{-\varepsilon_\lambda[C](l+\Delta l_\lambda)}}{I_0 e^{-\varepsilon_\lambda[C]l}}\right) = -\varepsilon_\lambda[C]\Delta l_\lambda \tag{5.3}$$

Taking the ratio of this equation at two wavelengths of light removes the dependence on $[C]$. Unlike the regular R derivation, the simplifying assumption that the Δl terms are equal cannot be made - movement of the probe may affect the path lengths of the two LEDs differently. The ε terms remain, because they are wavelength dependent.

$$R_N = \frac{-\varepsilon_{Red}[C]\Delta l_{Red}}{-\varepsilon_{IR}[C]\Delta l_{IR}} = \frac{\varepsilon_{Red}\Delta l_{Red}}{\varepsilon_{IR}\Delta l_{IR}} \tag{5.4}$$

The final R_N value is close to a constant. This constant is difficult to define analytically, as there are many tissues contributing to the catchall extinction coefficients ε_{Red} and ε_{IR}, including water, skin, fat and bone.

Since the red and infrared LEDs are not in the exact same position, the Δl terms in (5.4) for each wavelength will be closely related, but not identical. Therefore, this model expects a strong, but imperfect correlation between noise on the red and infrared channels. Consequently, some variance is introduced in the R_N calculations.

5.2.2 Blood Sloshing

This model assumes the predominant cause of motion-induced measurement bias is the result of blood movement that is unrelated to the cardiac cycle. As the hand accelerates, the blood's inertia causes it to resist any changes in motion, which can cause slight deformations in the capillaries, as illustrated in Fig. 5.2.

In a clean signal, the path length through the blood is modulated by the blood

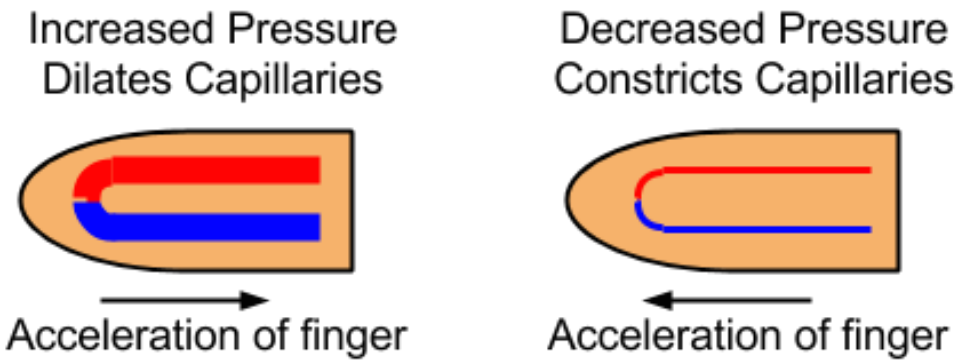

Figure 5.2: Illustration of the effect of blood momentum.

pressure changes induced by the cardiac cycle. In this model of motion artifact, the path length through the blood is modulated by the local blood pressure changes induced by movement. This effect may be more apparent in the venous blood than the arterial blood because of the lower blood pressure in the veins.

This type of blood movement can cause both arterial and venous blood to contribute to the PPG, in contrast to the motion-free PPG, which isolates arterial blood. In this model, it is assumed that R_N is caused solely by the movement of venous blood; movement of arterial blood contributes to R_S as if it was caused by the cardiac cycle.

The resulting R_N calculation in this model is identical to the R derivation in a clean signal; the difference is that since R_N is composed of venous blood, $[Hb]$ is greater and $[HbO_2]$ is less than the concentrations in arterial blood (5.5).

$$R_N = \frac{ln(I_p/I_t)_{Red}}{ln(I_p/I_t)_{IR}} = \frac{\varepsilon_{Hb,Red}[Hb] + \varepsilon_{HbO2,Red}[HbO_2]}{\varepsilon_{Hb,IR}[Hb] + \varepsilon_{HbO2,IR}[HbO_2]} \tag{5.5}$$

The final R_N value is a constant corresponding to the oxygen saturation of the venous blood. Although venous blood saturation depends on various physiological parameters, it is always less than arterial blood saturation. Therefore, R_N will be greater than R_S.

Since the red and infrared LEDs are not located in the exact same position in the probe, the amount of venous blood in the path between the LEDs and photodetector may be slightly different for each LED. Therefore, this model expects a strong, but imperfect correlation between noise on the red and infrared channels. Consequently, some variance will be introduced in the R_N calculations.

5.3 Analysis of Isolated Motion Artifact

Thirty seconds of isolated motion artifact signals were collected from each subject, as described in Section 3.2. Since analysis is being performed on isolated noise signals, calculated R values correspond to R_N.

Thirty seconds of clean PPG signals from each subject are used as a control, as described in Section 3.2. Calculated R values from the clean signals correspond to the R_S.

Samples of clean PPG and isolated noise are displayed in Fig. 5.3 for comparison. The clean PPG signals show strong correlation between red and infrared channels, while the isolated noise is less correlated. The amplitude of the isolated noise signals is shown at 10x the scale of the clean PPGs for visibility.

Characteristics of the control PPG and isolated motion artifact signals are presented in Table 5.1. The mean and standard deviation of R_S and R_N are presented, and converted to SpO_2 using the calibration curve in Section 3.3.1. The Pearson correlation coefficient (r) was calculated to check linear correlation between the red and infrared AC components.

The results in Table 5.1 show a clear difference in $\bar{x}_R$ and s_R between the control PPG and isolated motion artifact signals for each subject. The SpO_2 biases range

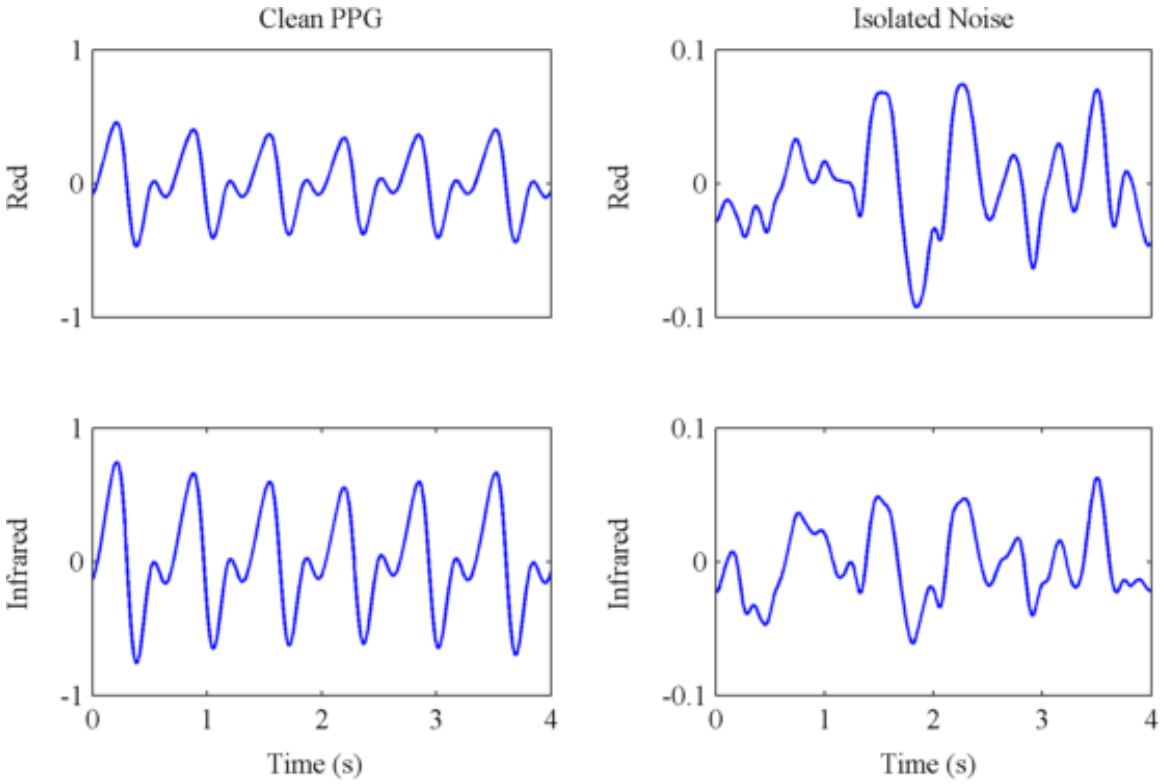

Figure 5.3: Samples from clean PPG and isolated noise signals. Amplitude of the isolated noise signals is shown at 10x the scale of the clean PPGs for visibility.

Table 5.1: Characteristics of Control and Isolated Motion Signals

	Control PPG					Isolated Motion Artifact				
	R_S		SpO_2 (%)		r	R_N		SpO_2 (%)		r
	$\bar{x}$	s	$\bar{x}$	s		$\bar{x}$	s	$\bar{x}$	s	
Subject 1	0.57	0.01	99.1	0.3	1.00	1.27	0.25	76.0	8.3	0.93
Subject 2	0.57	0.01	99.2	0.5	1.00	0.70	0.21	94.8	6.8	0.94
Subject 3	0.56	0.01	99.4	0.2	1.00	0.98	0.17	85.5	5.6	0.95
Subject 4	0.50	0.01	101.6	0.3	1.00	0.77	0.17	92.4	5.5	0.96
Subject 5	0.50	0.02	101.4	0.7	1.00	0.71	0.11	94.5	3.7	0.97

from 4% to 23%. Biases of this magnitude are considered clinically significant.

The Pearson correlation coefficient between the red and infrared channels is a perfect 1.00 in each subject in the control PPGs. The isolated noise signals show

strong ($r > 0.9$) but imperfect correlation between channels.

5.4 Discussion

The first model assumes that in pure noise, R_N is a constant defined by the ratio of red and infrared absorption coefficients. The values of these coefficients are difficult to determine experimentally, and will be dependent on individual physiology. Strong but imperfect correlation between channels is expected, due to the position of the LEDs in the probe.

The second model assumes that in pure noise, R_N is a constant defined by the oxygen saturation of the venous blood. Although the saturation of venous blood is lower than that of arterial blood, the degree to which they differ depends on individual physiology. Strong but imperfect correlation between channels is expected, due to the position of the LEDs in the probe.

While the two proposed models of motion artifact begin with different assumptions, they predict similar effects on the SpO_2 signal. Because the predicted effects are so similar, it is difficult to determine which model is correct, or if both models contribute simultaneously. The results presented in Table 5.1 provide evidence supporting both proposed motion artifact models; both models predicted R_N being different from R_S, and a decrease in correlation between red and infrared PPGs. However, they do not provide any evidence to distinguish the two.

Much of the work in the literature on pulse oximetry motion artifact focusses on software-based mitigation techniques. The models developed in this chapter, along with the experimental results, help illuminate some of the physical causes of motion artifact. This work may encourage hardware-based motion artifact mitigation strategies.

If steps are taken to minimize relative motion between the probe and the tissue, the effect of the varying path length model may be reduced. Furthermore, if the probe can be redesigned to ensure that the red and infrared LEDs share a source location, perhaps using prisms, the correlation of the red and infrared PPGs maybe be improved, reducing SpO_2 measurement variance.

Further research is indicated in validating these models, and assessing the contribution of each effect to PPG signal quality. This validation work should also be done using different types of probes. Theoretically the models should both apply to reflective probes as well as the transmissive probes used in this study. Any probe that may experience movement relative to the skin or movement of venous blood in the measurement field may be described by these models.

5.5 Chapter Summary

This chapter presented two physical models of motion artifact, and analytically derived their effects on the Beer-Lambert pulse oximetry model.

To experimentally verify the effects predicted by these models, the red-infrared correlation coefficient and the R mean and standard deviation were calculated using isolated motion artifact signals.

The experimental results showed evidence for the validity of both models, but insufficient evidence to distinguish between the two.

Chapter 6

Automatic Signal Quality Analysis

6.1 Introduction

The previous chapters examined some of the effects of motion artifact on the pulse oximetry readings. SpO_2 values were shown to lack precision and accuracy in the presence of motion artifact.

For diagnostic purposes, it is important to be able to detect poor quality pulse oximetry signals and reject them, rather than risk reporting incorrect measurements. This is particularly true in ambulatory monitoring settings, where noise is more prevalent. In fact, Lovell et al. identify automatic signal quality assessment as "An essential feature for unsupervised telehealth applications" [3]. Lovell et al. also note that despite the existing body of research in pulse oximetry motion artifact, little research exists to identify the cases where signal quality is so poor that accurate SpO_2 cannot be calculated [3].

This chapter seeks to perform an automatic signal quality analysis that can predict when a signal shows enough degradation to affect the SpO_2 estimate. To accomplish this goal, signal quality indices (SQIs) were established and calculated parallel to the SpO_2 calculation.

The following sections detail the development of three proposed SQI algorithms, the methodology employed to evaluate these algorithms, results of the evaluation and a discussion of the results.

6.2 Proposed SQI Algorithms

This section presents three proposed SQI algorithms. The following constraints were considered in developing the SQIs:

First, the SQI algorithms must rely solely on signals from the pulse oximeter with no help from external sensors. Relying on external hardware makes it more difficult to port the algorithms to various existing pulse oximeters; imposing this constraint ensures the algorithms remain relatively hardware agnostic.

Second, the algorithms must not rely on pulse detection, fiducial point detection or temporal alignment. Precise pulse segmentation and alignment is difficult in the presence of artifact. Precise fiducial point detection is also likely to fail during motion artifact. Ideally, the SQI calculations can be performed without depending on the success of pulse segmentation or fiducial point detection algorithms.

Finally, the SQIs must be calculated as often as possible - ideally as often as the SpO_2 is calculated (every second, in this thesis). This ensures a fast response time on the SQI signal to changing signal quality.

6.2.1 Preprocessing for SQI Calculation

The dataset underwent preprocessing steps common to all of the SQI algorithms described in this section. This preprocessing was similar to the steps described in Section 3.4.

Red, infrared, and two ambient light signals were low pass filtered at 5 Hz. The

AC components of each signal were isolated and normalized by the DC components. In Section 3.4, the frequency boundary between AC and DC components was set at 0.5 Hz - as high as possible without risking attenuation of the cardiac pulse frequency.

In the preprocessing for the SQIs, this boundary is set at 0.1 Hz. This is done to increase the sensitivity of the SQI algorithms by exposing them to noise below 0.5 Hz. SQIs were calculated over one-second non-overlapping windows.

6.2.2 Cross-Correlation of PPG Segments (SQI_{XCORR})

The first proposed SQI, SQI_{XCORR}, takes advantage of the quasi-periodicity of the PPG signal by cross-correlating incoming signal segments to previous segments. Previous work by Karlen et al. established a pulse oximetry SQI that relies on pulse segmentation and cross-correlation of incoming pulses with an ensemble average of previous pulses [27]. Quesnel et al. established a similar SQI for electrocardiogram signals by comparing incoming beats to an ensemble average of previous beats [37]. However, these approaches depend on beat detection and precise temporal alignment of subsequent pulses to establish the ensemble averaged template. Automatic detection and alignment of PPG pulses can be difficult in noisy conditions. SQI_{XCORR} performs its analysis without the need for beat detection.

To calculate SQI_{XCORR}, the infrared PPG signal is preprocessed as described in Section 6.2.1. For each one-second PPG segment being tested, a template segment is defined as the two-second PPG segment immediately prior to the test segment. By using a two-second template, it can be ensured that the pulses in the complete one-second test segment can be aligned with a portion of the template segment.

The template segment and test segment are normalized by their means and standard deviations to ensure that the cross-correlation calculation is affected only by changes in waveform shape, and not amplitude. These calculations are shown in

(6.1), where X and Y are the test and template PPG vectors, μ is mean and σ is standard deviation.

$$\begin{aligned} X_{NORM} &= (X - \mu_X)/\sigma_X \\ Y_{NORM} &= (Y - \mu_Y)/\sigma_Y \end{aligned} \tag{6.1}$$

Since the cross-correlation is a function of time delay, the maximum of this function will provide a measure of similarity at the point where the two signals are best aligned.

The cross-correlation between the test and template segments is calculated in (6.2), where m is the sample index in the segments and $\rho_{XY}[n]$ is the cross-correlation as a function of time delay n between the segments.

$$max(\rho_{XY}[n]) = max\left(\sum_{m=0}^{2fs}(X_{NORM}[m])(Y_{NORM}[m+n])\right) \tag{6.2}$$

The maximum cross-correlation needs to be compared to a point of reference representing the maximum possible signal quality. This is generated by calculating the maximum value of the autocorrelation of the two-second template segment ($max(\rho_{YY})$), and dividing by two to correct it to a one-second equivalent. The equation is similar to (6.2), but since the maximum of the autocorrelation of a signal occurs at a time shift $n = 0$, it can be simplified (6.3).

$$max(\rho_{YY}[n])/2 = \left(\sum_{m=0}^{2fs}(Y_{NORM}[m])^2\right)/2 \tag{6.3}$$

The final SQI_{XCORR} metric is defined in (6.4). This approach assumes that the motion artifact noise in X and Y are poorly correlated.

$$SQI_{XCORR} = \frac{2max(\rho_{XY})}{max(\rho_{YY})} \tag{6.4}$$

6.2.3 AC Power of Ambient Light SQI_{AMB}

By visual inspection, the ambient light signal is affected by motion artifact. This effect is apparent in Fig. 6.1. The ambient signal associated with the clean PPG is a relatively steady DC value, while the ambient signal associated with the contaminated PPG shows AC contamination of its own. When a subject moves, relative motion between the probe and the finger can modulate the ambient light leakage to the photodetector.

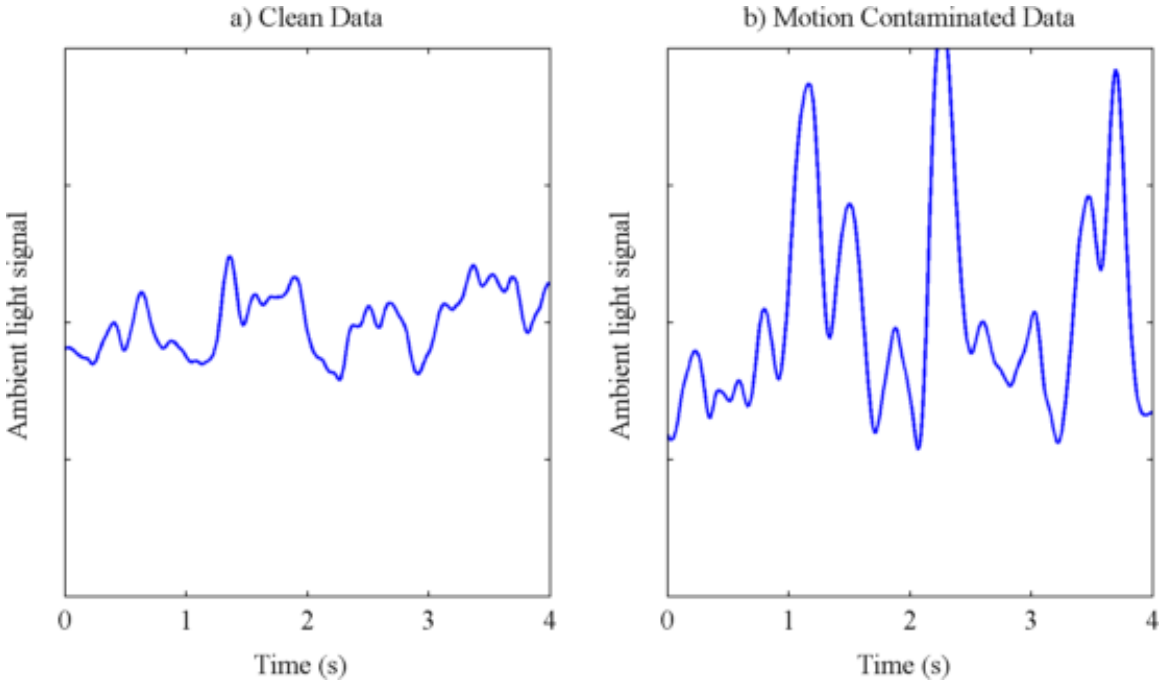

Figure 6.1: Effect of motion on ambient light signal. Signals are low pass filtered at 5 Hz.

It is hypothesized that this property can be used to detect motion artifact in the PPG signal. The proposed SQI (SQI_{AMB}) is calculated using the infrared PPG and

associated ambient light signal, as described in (6.5). For each signal segment, the AC components of the PPG and ambient light signals are isolated and normalized by their DC components. The reported SQI is the ratio of the RMS amplitudes of the normalized PPG and ambient light signals. This SQI is expressed in decibels, because the amplitude of the PPG is much greater than the amplitude of the ambient light signal. Calculating the logarithm amplifies the effect of small increases in the ambient light signal.

$$SQI_{AMB} = 20log_{10}\left(\frac{RMS(AC_{IR}/DC_{IR})}{RMS(AC_{IRamb}/DC_{IRamb})}\right) \tag{6.5}$$

6.2.4 Correlation of Red and Infrared PPGs (SQI_{RICORR})

As demonstrated in Section 5.3, clean PPG signals have near-perfect linear correlation between the red and infrared PPGs. This correlation is decreased in the isolated motion artifact signal.

It is hypothesized that this property can be use to detect motion artifact in the PPG signal. The proposed SQI (SQI_{RICORR}) is calculated using the red and infrared PPG signals, as described in (6.6). For each signal segment, the AC components of the PPGs are isolated and normalized by their DC components. The reported SQI in (6.6) is the Pearson Correlation Coefficient (r), where x and y are red and infrared PPGs, respectively, $\bar{x}$ and $\bar{y}$ are means, and σ_x and σ_y are standard deviations.

$$SQI_{RICORR} = r = \frac{\sum(x_i - \bar{x})(y_i - \bar{y})}{\sigma_x \sigma_y} \tag{6.6}$$

6.3 Methodology

6.3.1 Real Contaminated Data

The SQI algorithms were tested on the PPG signals collected from each subject. Although the movement conditions were not strictly controlled and are not necessarily comparable between subjects, a successful SQI algorithm should show a general negative trend with increasing movement intensity.

An SQI is calculated for each one-second segment of each test signal. The mean and standard deviation of the SQIs in each movement condition for each subject are calculated.

The performance of each SQI algorithm was tested on two binary classification problems - motionless vs. low motion PPG, and motionless vs. high motion PPG. This test was done using the data pooled from all subjects.

Finally, a Spearman rank correlation coefficient was calculated for each SQI algorithm, to test for a monotonic correlation between SQI and movement intensity.

6.3.2 Artificially Contaminated Data

The artificially contaminated data was used to examine the relationship between the true SNR and SQI scores. After DC normalization, the AC portion of the isolated noise signals were scaled and added to the AC portion of clean PPGs.

The true SNR for each one-second signal segment was calculated according to (6.7):

$$SNR = 20log_{10}\left(\frac{AC_{IR}/DC_{IR}}{k * (AC_{IRnoise}/DC_{IRnoise})}\right) \tag{6.7}$$

SQI_{XCORR} and SQI_{RICORR} scores were calculated and tested for a monotonic

correlation with the true SNR using Spearman's rank correlation coefficient. SQI_{AMB} is not evaluated with this methodology, as the SQI score is directly related to the AC amplitude of the ambient light signal, which is artificially scaled in the contamination process.

6.4 Results

6.4.1 Real Contaminated Data

For each SQI algorithm, mean and standard deviation of the SQIs across all subjects are calculated. The scores for SQI_{XCORR}, SQI_{AMB} and SQI_{RICORR} are displayed in Fig. 6.2. The mean and standard deviation of SQI scores for each subject and each movement condition are reported in Appendix B. All three SQI algorithms successfully discriminate between motionless and movement conditions, but do not discriminate between the three levels of motion tested.

The strength of the monotonic correlation between SQI scores and movement intensity was evaluated for each algorithm using Spearman's rank correlation coefficient (r_S). The results are displayed in Table 6.1. All three algorithms showed weak monotonic relationships with movement intensity.

Table 6.1: Spearman's rank correlation between SQI and movement intensity

SQI Algorithm	r_S
SQI_{XCORR}	0.33
SQI_{AMB}	0.49
SQI_{RICORR}	0.49

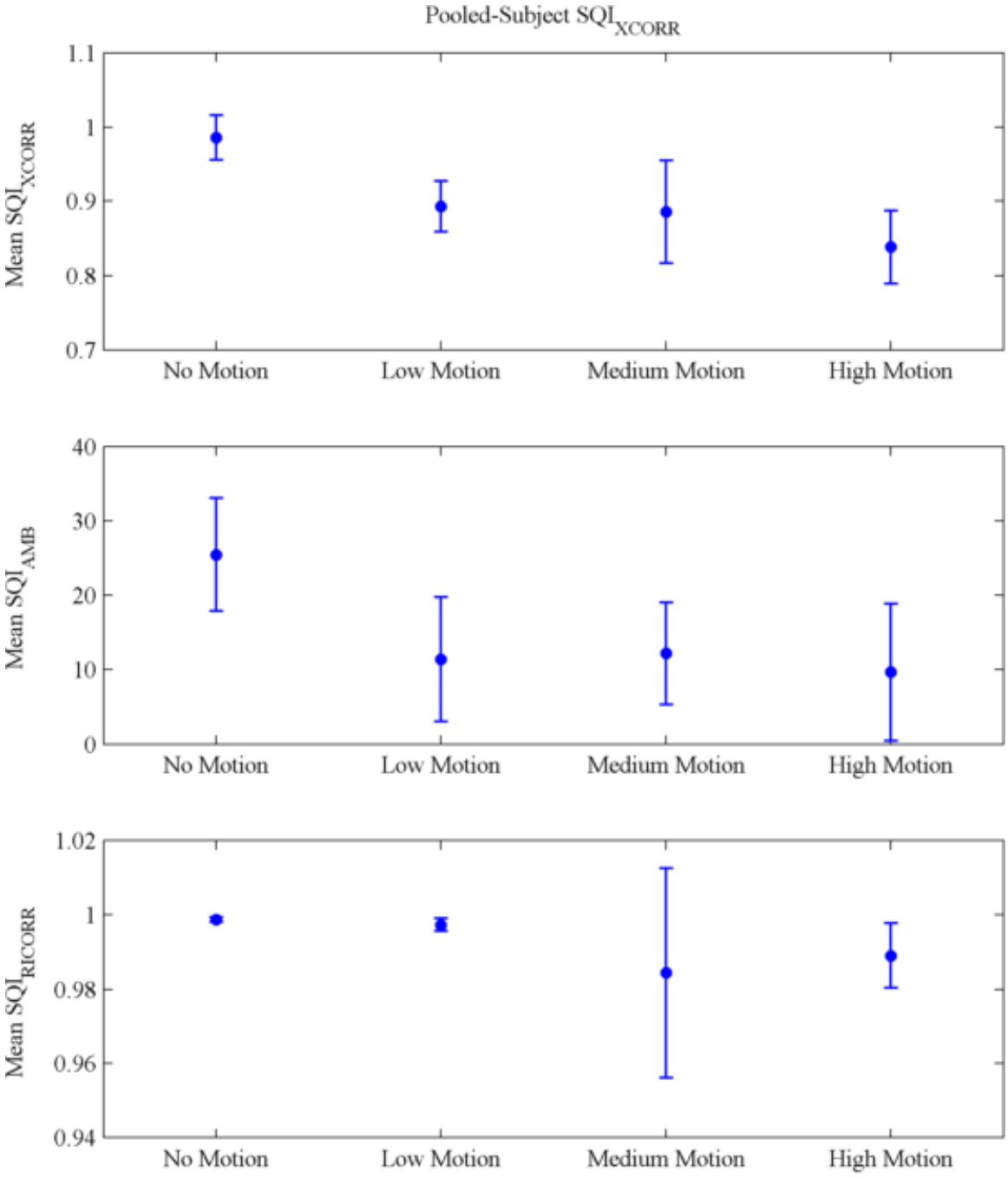

Figure 6.2: Comparison of SQI subject means in real motion contaminated data. Error bars represent standard deviation of subject means.

The receiver operating characteristic (ROC) curves for classification between motionless and high motion are presented in Fig. 6.3. SQI_{AMB} had the greatest performance across threshold levels with an area under the curve of $AUC = 0.91$. SQI_{RICORR} and SQI_{XCORR} followed, with $AUC = 0.88$ and $AUC = 0.84$ respectively. At some specific thresholds (false positive rate 0.2-0.4), the performance of SQI_{RICORR} exceeds that of SQI_{AMB}.

The ROC curves for classification between motionless and low motion are presented in Fig. 6.4. Again, SQI_{AMB} had the highest greatest performance across threshold levels with an area under curve of $AUC = 0.90$. SQI_{XCORR} and SQI_{RICORR} followed, with $AUC = 0.71$ and $AUC = 0.67$ respectively. SQI_{AMB} also had the most consistent performance, while SQI_{XCORR} and SQI_RICORR both performed worse in the low movement condition.

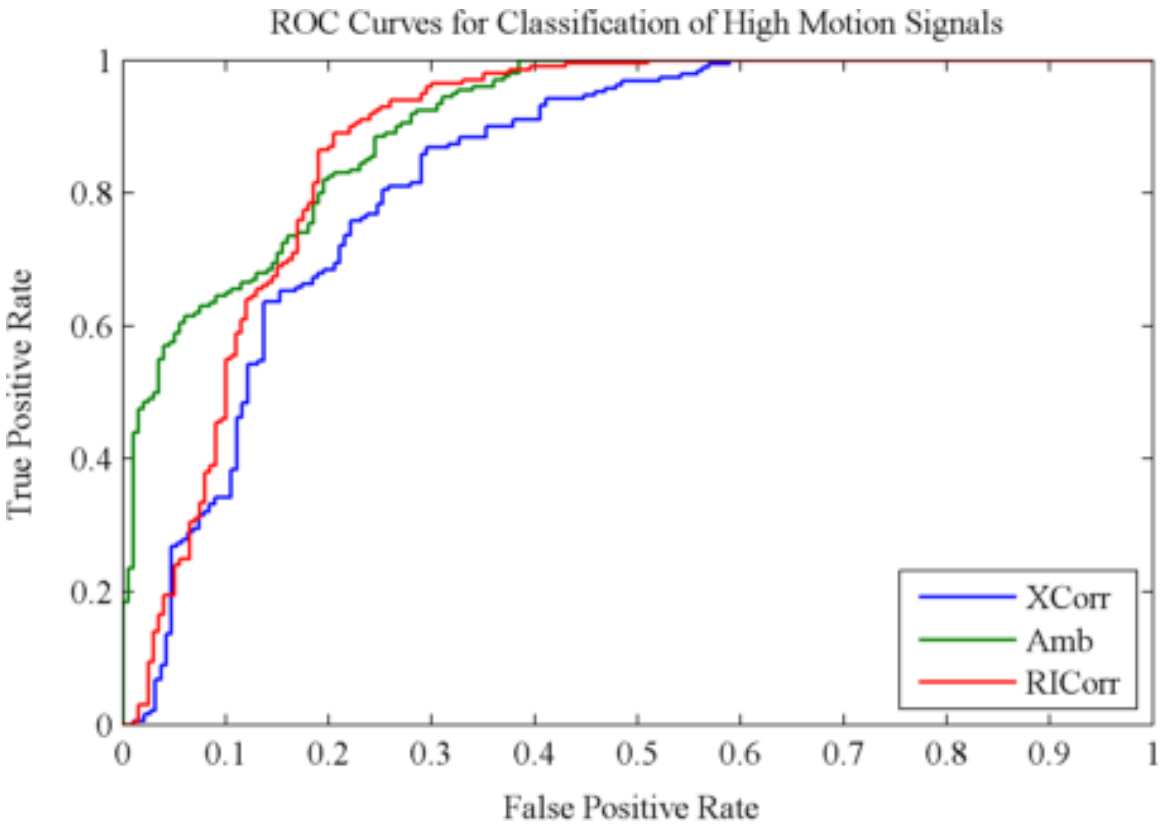

Figure 6.3: ROC curves for classification of motionless and high motion data.

To demonstrate implementation of SpO_2 calculation with parallel SQI, an example signal was generated using segments of real data from one subject. The signal consists of ten seconds motionless, ten seconds of low motion, ten seconds motionless and ten seconds of high motion. SpO_2 calculations are shown with SQI scores from each algorithm in Fig. 6.5. No shading indicates motionless data, yellow indicates low motion and green indicates high motion. Periods of motion are marked by an increase in SpO_2 variance. SQI_{AMB} decreases significantly for both movement conditions but does not discriminate between the two. SQI_{RICORR} decreases slightly for the low motion condition and significantly for the high motion. SQI_{XCORR} decreases slightly for the movement conditions but does not strongly discriminate between the two.

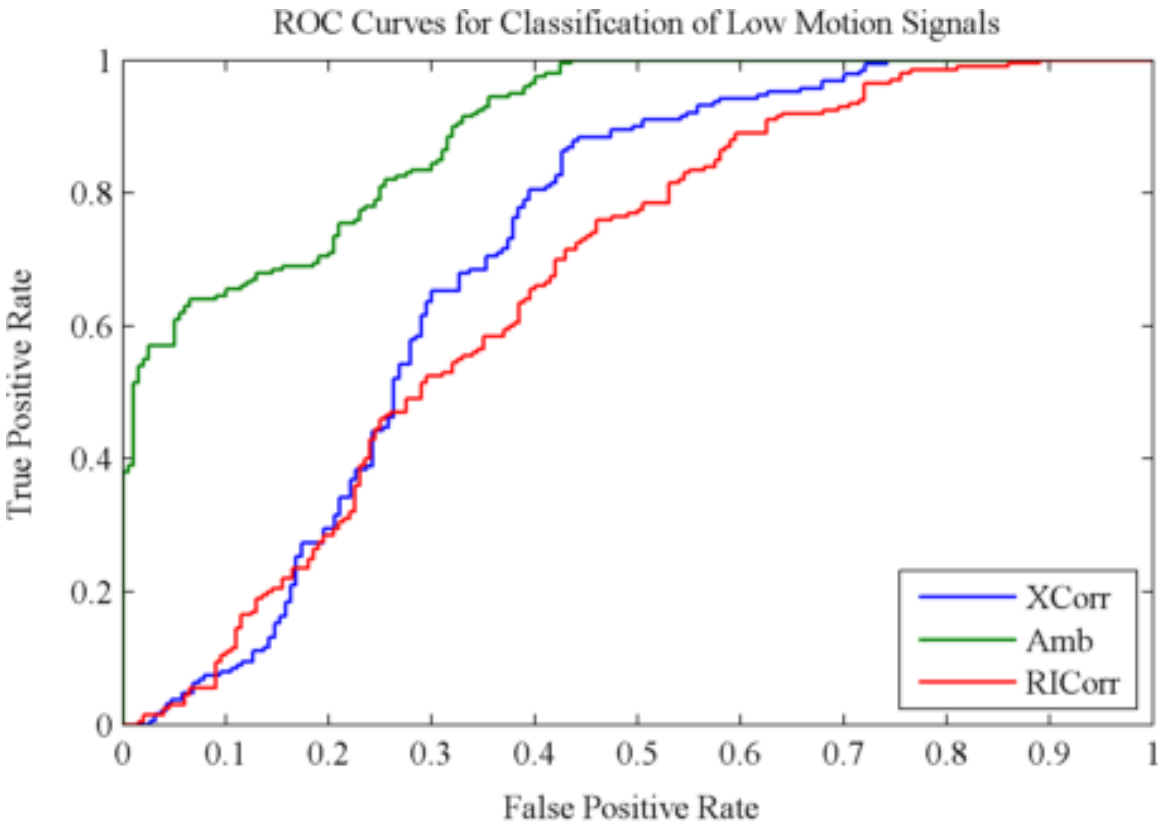

Figure 6.4: ROC curves for classification of motionless and low motion data.

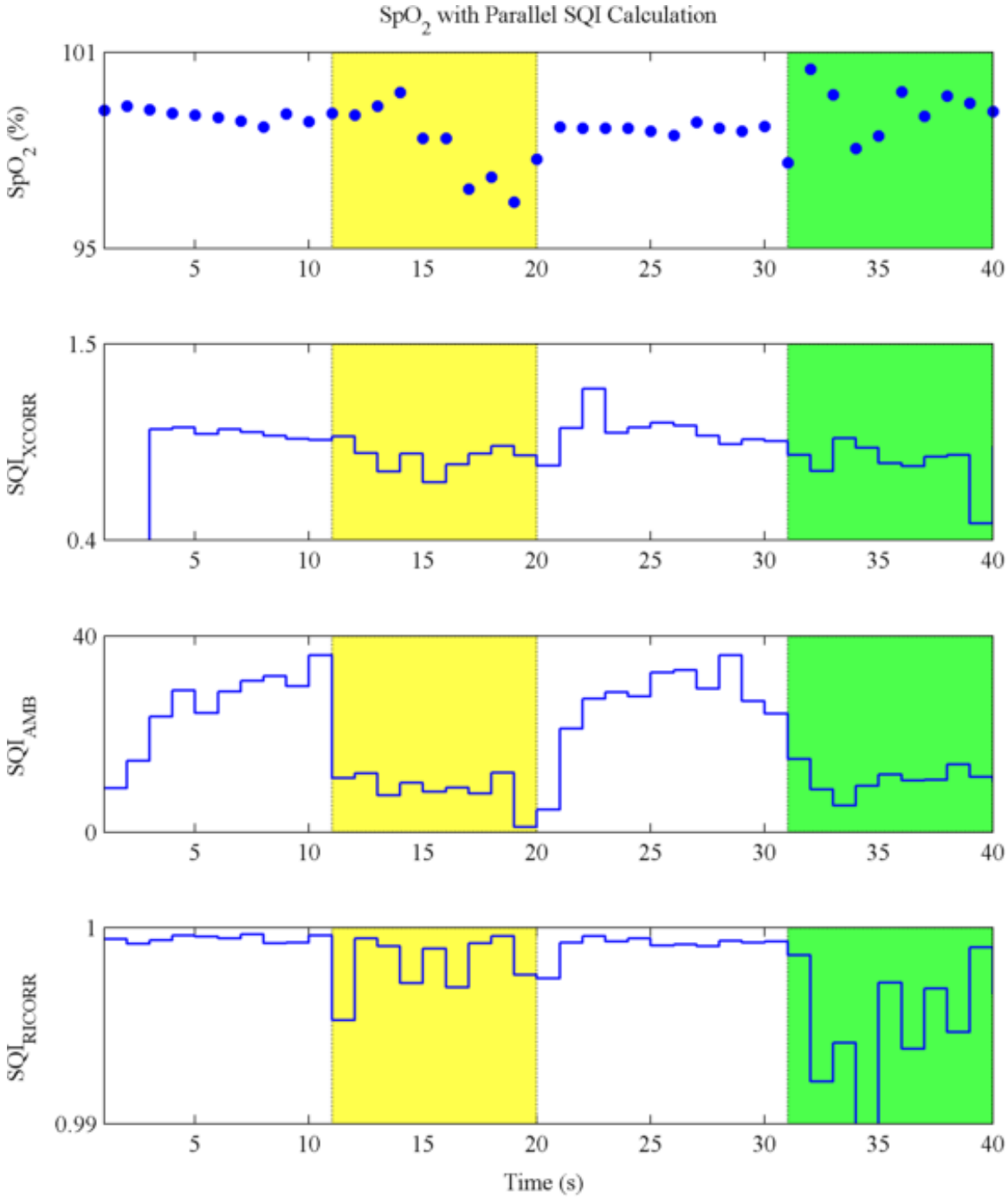

Figure 6.5: SpO_2 calculation with parallel SQIs. No shading indicates motionless data, yellow indicates low motion and green indicates high motion.

6.4.2 Artificially Contaminated Data

Pooled-subject scatterplots of SNR vs. SQI using the artificially contaminated data set are presented for SQI_{XCORR} and SQI_{RICORR} in Fig. 6.6 and Fig. 6.7 respectively. SQI_{XCORR} and SQI_{RICORR} scores show positive monotonic correlation with SNR, $r_S = 0.66$ and $r_S = 0.54$ respectively.

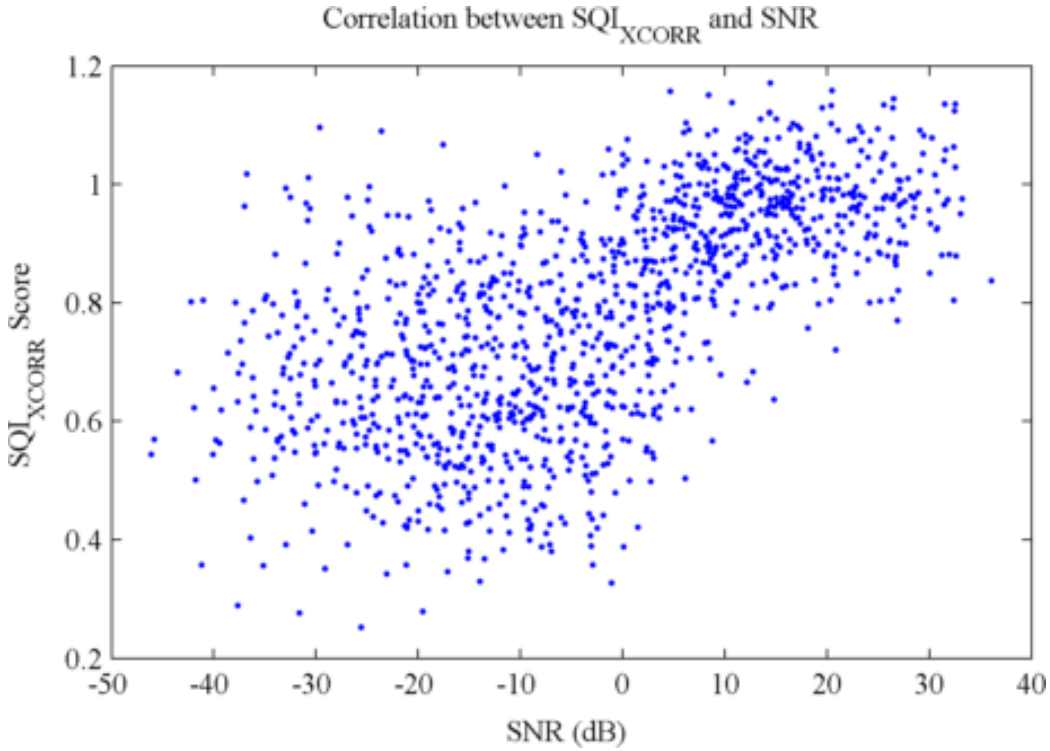

Figure 6.6: Correlation between SQI_{XCORR} and SNR in artificially contaminated data. Each point represents SQI_{XCORR} and SNR calculated for a single one-second PPG segment.

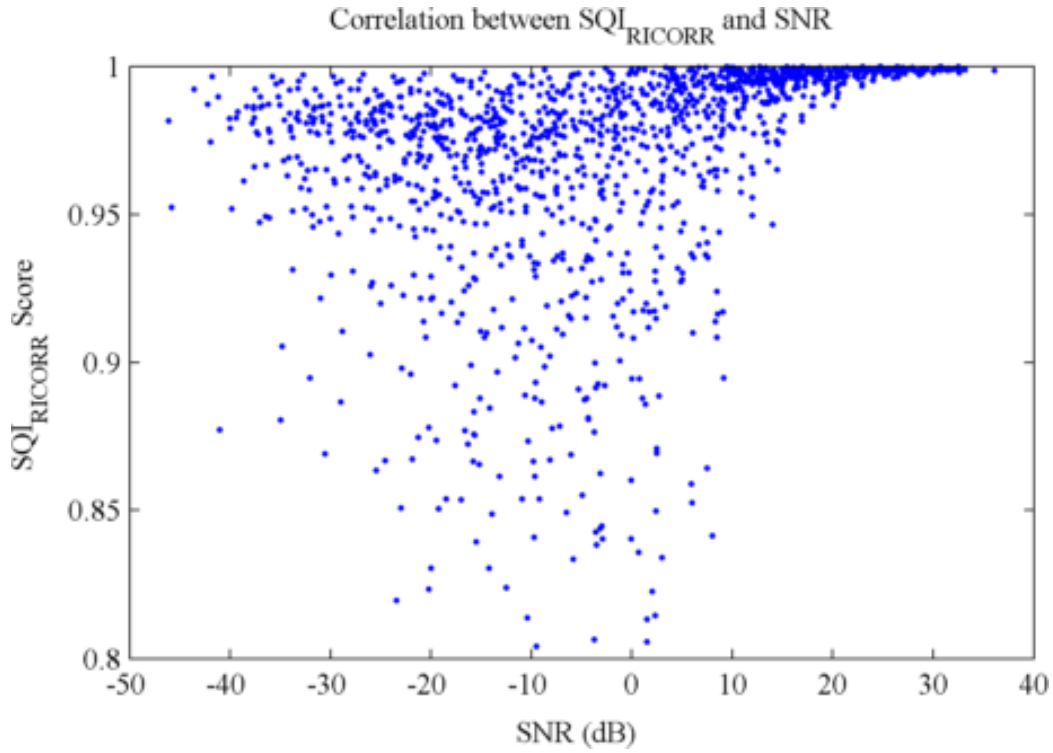

Figure 6.7: Correlation between SQI_{RICORR} and SNR in artificially contaminated data. Each point represents SQI_{RICORR} and SNR calculated for a single one-second PPG segment.

6.5 Discussion

All three proposed algorithms met the criteria stated in Section 6.2. They rely solely on signals produced by standard pulse oximeters, they do not rely on fiducial point detection or temporal pulse alignment, and they are calculated every second. SQI_{XCORR} requires two seconds of reference data before the first SQI can be calculated on the third second, but SQI_{AMB} and SQI_{RICORR} can begin reporting scores immediately.

The proposed SQI algorithms were shown to successfully discriminate between motionless and movement conditions. SQI_{AMB} showed the best overall performance in both binary classification tasks, with very little performance loss when the motion intensity was reduced. All three algorithms showed weak monotonic relationships between SQI and movement intensity, as indicated by Spearman's rank correlation

coefficient.

In clinical applications, an SQI may be used to mask false alarms caused by low signal quality. In this scenario, falsely identifying a segment as being contaminated is costly and could lead to masking true alarms. To avoid this, the false positive rate should be minimized. At thresholds that minimize false positives, SQI_{AMB} performs particularly well. Outside the clinical environment, the tradeoff between true positive rate and false positive rate is application specific, and can be tuned by adjusting the SQI threshold.

SQI_{XCORR} and SQI_{RICORR} were tested for correlation with true SNR in artificially contaminated signals. SQI_{XCORR} showed a stronger monotonic relationship with true SNR ($r_S = 0.66$) than SQI_{RICORR} ($r_S = 0.54$), which indicates that SQI_{XCORR} may be better at quantifying motion artifact, rather than just detecting it.

The one-second buffer for SQI calculations ideally included at least one complete PPG pulse. This would not be the case for subjects with heart rates below 60 bpm. Since SQI_{AMB} and SQI_{RICORR} do not rely on the periodicity of the PPG signal, they would likely be relatively unaffected by low heart rates. SQI_{XCORR} would likely see a performance decrease, as incomplete segments would be more likely to generate spurious correlations.

Similar to calculation of SpO_2, SQI calculation may benefit from averaging measurements over a longer period of time. Implementing a rolling average of several SQI calculations could mitigate some of the variance in the calculations. However, these techniques would lead to a system that is less responsive to sudden changes in SQI. The trade-off between SQI accuracy and responsiveness could be tuneable in a real system, and this threshold would likely be application specific.

In real life applications, the SQI threshold adjustment cannot be considered in

isolation. Two binary classification problems need to be approached in sequence. The first problem was addressed in this chapter - "Is the given PPG segment of sufficient quality to be further analyzed?". If the signal has sufficient quality, the second problem is "Should the given PPG segment trigger an alarm?". The thresholds for these two classifiers must be considered in tandem to reduce the false alarm rate of the overall system. This approach has precedent in the biometric security industry, where a system must first decide if a reasonable quality biometric sample has been recorded before an authentication decision can be made [38].

Further research is indicated in correlating SQI scores with SpO_2 measurement uncertainty. Since different applications have different levels of acceptable SpO_2 error, understanding the relationship between SQI and SpO_2 error is necessary to set appropriate classification thresholds. This work may need to be repeated for different types of pulse oximeter probes. While transmissive and reflective probes generate very similar PPG waveforms, they may react differently to motion and alter the PPG waveform in unique ways.

Further research may also be indicated in using supplemental signals to determine SQI. For example, an accelerometer on the probe would give an indication of motion intensity. Supplemental electrocardiogram signals could help identify individual pulses to do a pulse-by-pulse SQI calculation. The downside to this approach is the extra hardware and software complexity needed. The techniques proposed in this thesis can be implemented in existing pulse oximetry hardware with minimal impact on complexity and ease of use.

Unfortunately, there is no way to implement these proposed SQI algorithms on existing pulse oximeters, as they all require access to the raw signals being measured. Implementation in a clinical environment would require integration by a partner pulse oximeter manufacturer, where an SQI level could be calculated and displayed on the

device alongside SpO_2, as well as integrated into the alarm settings.

6.6 Chapter Summary

This chapter presented three automatic signal quality assessment algorithms, which were then evaluated by their ability to classify clean and motion contaminated data. Two of the algorithms were evaluated for correlation with true SNR in artificially contaminated signals.

SQI_{AMB} demonstrated the best performance in classifying clean and motion contaminated PPGs. Its performance was not significantly degraded when the classification challenge was increased by using the low motion signals. SQI_{XCORR} and SQI_{RICORR} both performed reasonably well in identifying high motion signals, but classification performance was degraded for the low motion signals.

Further study is indicated to correlate SQI scores with SpO_2 measurement uncertainty to help determine appropriate application-specific classification thresholds.

Chapter 7

Conclusions and Future Work

In this thesis, the signal quality challenges facing ambulatory pulse oximetry monitoring were addressed. This included exploring the effects of motion artifact on SpO_2 measurements, modelling proposed origins of motion artifact, and developing automatic signal quality assessment algorithms.

7.1 Summary of Findings

7.1.1 Effects of Motion Artifact on SpO_2 Measurement

Previous work has demonstrated measurement error associated with motion artifact in pulse oximetry [5, 6]. The size of this error is dependent on the parameters of the specific SpO_2 calculation algorithms employed, and the characteristics and intensity of motion artifact. In their meta analysis of motion-resistant pulse oximeters, Giuliano et al. noted a lack of consistency in motion artifact generation methodology [31].

In Chapter 4, measurement bias and variance in a set of motion contaminated signals was evaluated using the conventional SpO_2 calculation algorithm. While the results suggested motion artifact could cause inaccurate SpO_2 measurements, the data did not support findings of a systematic negative bias reported in previous literature.

SpO_2 measurement bias and variance were also evaluated as a function of signal to noise ratio in artificially contaminated signals. These results showed evidence for a negative SpO_2 bias at low signal to noise ratios.

The discrepancy between results using real data and artificially contaminated data is notable. It is likely that that the real data collected in this study did not simulate sufficiently low SNRs to show the trend identified in the artificial contamination model and in previous literature.

7.1.2 Analytical Models of Pulse Oximetry Motion Artifact

Two hypotheses for the source of motion artifact are discussed in the literature [8], and were further explored in Chapter 5. The models developed in Chapter 5 started with a proposed motion artifact origin, and derived the effects of the origin on the SpO_2 calculation algorithm. The predicted effects were compared to real isolated motion artifact signals.

Both models predicted SpO_2 measurement bias and an increase in variance in motion contaminated signals. The results showed evidence for a negative SpO_2 bias and an increase in variance. Furthermore, the results support both models of motion artifact - the varying path length model and the blood sloshing model. The results presented no evidence to distinguish the two models, but it is plausible that both contribute to the motion artifact signal.

7.1.3 Automatic Signal Quality Assessment

Three automatic signal quality assessment algorithms were developed with the goal of facilitating implementation on existing pulse oximeters. In order to achieve this goal, the algorithms were designed to rely solely on the signals generated by the pulse

oximeter, and do not require external sensors. They do not rely on beat detection, fiducial point detection, or precise temporal alignment of pulses. Finally, to ensure rapid reaction to changes in signal quality, scores were generated for every one-second segment of the PPG.

All three SQI algorithms performed well classifying motionless vs. high motion signals. The SQI_{AMB} algorithm maintained its level of performance when classifying low motion signals, while SQI_{XCORR} and SQI_{RICORR} showed reduced performance. None of the algorithms were able to differentiate between the three different movement conditions. All three algorithms demonstrated weak monotonic relationships between SQI and movement intensity. These issues with the SQI algorithms may be caused by lack of differentiation of the movement intensity levels in the data.

SQI_{XCORR} and SQI_{RICORR} were also tested for correlation with true SNR in artificially contaminated signals. Despite their similar performance in the binary classification problem, SQI_{XCORR} showed a stronger monotonic relationship with true SNR.

7.2 Implications for Future Work

7.2.1 Effects of Motion Artifact on SpO_2 Measurement

Both the real and artificially contaminated data showed evidence of inaccurate SpO_2 measurements during periods of motion. In the hospital, clinicians using pulse oximetry are taught to make subjective evaluations of the PPG tracing when interpreting SpO_2 data. In many remote monitoring applications, this subjective analysis of signal quality is lost. Since signal quality is strongly linked to SpO_2 accuracy, parallel signal quality assessment algorithms are indicated in applications where subjective assessment by a clinician is infeasible.

Further study is indicated in developing methodologies to evaluate motion resistant pulse oximetry and signal quality assessment algorithms. This thesis noted issues in characterizing, quantifying and reproducing clinically significant motion artifact.

7.2.2 Analytical Models of Pulse Oximetry Motion Artifact

Researching the mechanisms of motion artifact is an important exercise. Much of the research in pulse oximetry motion artifact focusses on mitigation in post-processing algorithms. However, a better understanding of the origins of motion artifact may influence research into mitigation at the source.

The models suggest design considerations for motion artifact resistant probes. To minimize the relative movement between the probe and the finger, lightweight, flexible, snugly-fitting probes are indicated. To minimize the effects of the offset red and infrared LEDs, prisms can be employed to ensure that incident light from the two LEDs follows the exact same path.

7.2.3 Automatic Signal Quality Assessment

All three proposed SQIs were shown to discriminate between motionless and motion conditions in the dataset. However, they may fail to quantify the intensity of motion artifact. This was evidenced by poor discrimination between motion conditions in the real data, weak correlations between SQI and movement intensity, and the weak correlations of SQI_{XCORR} and SQI_{RICORR} to SNR in the artificially contaminated data.

Further research is indicated in understanding the relationship between SQI scores and SpO_2 measurement uncertainty. Understanding this relationship is necessary to establish appropriate application-specific classification thresholds.

List of References

[1] World Health Organization, "World health statistics 2013: a wealth of information on global public health." WHO Press, 2013.

[2] N. Oljaca, "Advances in bio-inspired sensing help people lead healthier lives," tech. rep., Texas Instruments, Aug. 2014.

[3] N. H. Lovell, S. J. Redmond, J. Basilakis, and B. G. Celler, "Biosignal quality detection: An essential feature for unsupervised telehealth applications," in *e-Health Networking Applications and Services (Healthcom), 2010 12th IEEE International Conference on*, pp. 81–85, IEEE, 2010.

[4] A. Pantelopoulos and N. G. Bourbakis, "A Survey on Wearable Sensor-Based Systems for Health Monitoring and Prognosis," *Systems, Man, and Cybernetics, Part C: Applications and Reviews, IEEE Transactions on*, vol. 40, no. 1, pp. 1–12, 2010.

[5] S. J. Barker and N. K. Shah, "The Effects of Motion on the Performance of Pulse Oximeters in Volunteers (Revised publication)," *Anesthesiology*, vol. 86, p. 101, Jan. 1997.

[6] S. T. Lawless, "Crying wolf: false alarms in a pediatric intensive care unit," *Critical Care Medicine*, vol. 22, pp. 981–985, June 1994.

[7] G. D. Fraser, A. D. C. Chan, J. R. Green, and D. T. MacIsaac, "Automated Biosignal Quality Analysis for Electromyography Using a One-Class Support Vector Machine," *Instrumentation and Measurement, IEEE Transactions on*, vol. 63, no. 12, pp. 2919–2930, 2014.

[8] J. M. Goldman, M. T. Petterson, R. J. Kopotic, and S. J. Barker, "Masimo Signal Extraction Pulse Oximetry," *Journal of Clinical Monitoring and Computing*, vol. 16, no. 7, pp. 475–483, 2000.

[9] G. W. J. Clarke, A. D. C. Chan, and A. Adler, "Effects of motion artifact on the blood oxygen saturation estimate in pulse oximetry," *Medical Measurements and Applications (MeMeA), 2014 IEEE International Symposium on*, pp. 1–4, 2014.

[10] G. W. J. Clarke, A. D. C. Chan, and A. Adler, "Quantifying Blood-Oxygen Saturation Measurement Error in Motion Contaminated Pulse Oximetry Signals," *World Congress on Medical Physics and Biomedical Engineering*, 2015.

[11] User: Helix84, "Gaseous Exchange in the Lung." Wikimedia Commons, CC-BY-SA-3.0.

[12] J. G. Webster, "Design of pulse oximeters." Taylor & Francis Group, New York, 1997.

[13] A. Curtin, "Absorption spectra of oxygenated hemoglobin (HbO2) and deoxygenated hemoglobin (Hb) for Near-infrared wavelengths (NIR)." Wikimedia Commons, CC-BY-SA-3.0.

[14] M. Nitzan, S. Noach, E. Tobal, Y. Adar, Y. Miller, and E. Shalom, "Calibration-Free Pulse Oximetry Based on Two Wavelengths in the Infrared—A Preliminary Study," *Sensors*, 2014.

[15] J. G. Kim and H. Liu, "Variation of haemoglobin extinction coefficients can cause errors in the determination of haemoglobin concentration measured by near-infrared spectroscopy," *Physics in medicine and biology*, 2007.

[16] Johns Hopkins Medicine Health Library, "Oximetry," *hopkinsmedicine.org - Accessed March 2015*.

[17] R. P. Garrido-Chamorro, "Desaturation patterns detected by oximetry in a large population of athletes," *Research quarterly for exercise and sport*, 2009.

[18] P. Peeling and R. Andersson, "Effect of hyperoxia during the rest periods of interval training on perceptual recovery and oxygen re-saturation time," *Journal of Sports Sciences*, 2011.

[19] L. J. Mengelkoch, D. Martin, and J. Lawler, "A Review of the Principles of Pulse Oximetry and Accuracy of Pulse Oximeter Estimates During Exercise," *Physical therapy*, vol. 74, pp. 40–49, Jan. 1994.

[20] ECRI Institute, "Top 10 Health Technology Hazards for 2015," *Health Devices*, pp. 1–33, Nov. 2014.

[21] R. K. Avent and J. D. Charlton, "A critical review of trend-detection methodologies for biomedical monitoring systems.," *Critical reviews in biomedical engineering*, 1989.

[22] M. C. Chambrin, "Alarms in the intensive care unit: how can the number of false alarms be reduced?," *CRITICAL CARE-LONDON-*, 2001.

[23] S. Nizami, J. R. Green, and C. McGregor, "Implementation of Artifact Detection in Critical Care: A Methodological Review," *Biomedical Engineering, IEEE Reviews in*, vol. 6, pp. 127–142, 2013.

[24] L. Wiklund, B. Hok, K. Ståhl, and A. Jordeby-Jönsson, "Postanesthesia monitoring revisited: Frequency of true and false alarms from different monitoring devices," *Journal of Clinical Anesthesia*, vol. 6, pp. 182–188, May 1994.

[25] M. T. Petterson and V. L. Begnoche, "The effect of motion on pulse oximetry and its clinical significance," *Anesthesia & Analgesia*, 2007.

[26] J. A. Sukor, S. J. Redmond, and N. H. Lovell, "Signal quality measures for pulse oximetry through waveform morphology analysis," *Physiological measurement*, vol. 32, pp. 369–384, Mar. 2011.

[27] W. Karlen, K. Kobayashi, and J. M. Ansermino, "Photoplethysmogram signal quality estimation using repeated Gaussian filters and cross-correlation," *Physiological ...*, 2012.

[28] Q. Li and G. D. Clifford, "Dynamic time warping and machine learning for signal quality assessment of pulsatile signals," *Physiological measurement*, vol. 33, pp. 1491–1501, Aug. 2012.

[29] I. Silva, J. Lee, and R. G. Mark, "Signal Quality Estimation With Multichannel Adaptive Filtering in Intensive Care Settings," *Biomedical Engineering, IEEE Transactions on*, vol. 59, no. 9, pp. 2476–2485, 2012.

[30] K. A. Reddy, B. George, N. M. Mohan, and V. J. Kumar, "A Novel Calibration-Free Method of Measurement of Oxygen Saturation in Arterial Blood," *Instrumentation and Measurement, IEEE Transactions on*, vol. 58, no. 5, pp. 1699–1705, 2009.

[31] K. K. Giuliano and T. L. Higgins, "New-Generation Pulse Oximetry in the Care of Critically Ill Patients," *American Journal of Critical Care*, vol. 14, pp. 26–37, Jan. 2005.

[32] P. D. Mannheimer and C. R. Baker, "Digital Signal Processing Technology in Nellcor OxiMax Pulse Oximeters," tech. rep., Apr. 2011.

[33] Texas Instruments, "AFE4400 Integrated Analog Front-End for Heart Rate Monitors and Low-Cost Pulse Oximeters," July 2014.

[34] P. K. B. C. Raju, "Arterial Tourniquets - Anaesthesia Tutorial of the Week," tech. rep., Oct. 2010.

[35] T. T. Horlocker, J. R. Hebl, B. Gali, and C. J. Jankowski, "Anesthetic, patient, and surgical risk factors for neurologic complications after prolonged total tourniquet time during total knee arthroplasty," *Anesthesia & ...*, 2006.

[36] N. Stuban and M. Niwayama, "Optimal filter bandwidth for pulse oximetry," *Review of Scientific Instruments*, vol. 83, no. 10, pp. 104708–104708, 2012.

[37] P. X. Quesnel, A. D. C. Chan, and H. Yang, "Signal quality and false myocardial ischemia alarms in ambulatory electrocardiograms," *Medical Measurements and Applications (MeMeA), 2014 IEEE International Symposium on*, pp. 1–5, 2014.

[38] A. Adler and S. A. C. Schuckers, "Security and Liveness, Overview," in *Encyclopedia of Biometrics*, pp. 1–9, Boston, MA: Springer US, May 2014.

Appendix A

Derivation of SpO_2 from Beer-Lambert Law

The goal is to derive SpO_2, the percentage of haemoglobin that is saturated with oxygen. $[HbO_2]$ and $[Hb]$ are the molar concentrations of oxygenated and deoxygenated haemoglobin, respectively.

$$SpO_2 = \frac{[HbO_2]}{[HbO_2] + [Hb]} \times 100\% \tag{A.1}$$

A.1 Beer-Lambert Model

The Beer-Lambert law describes the attenuation of light transmitted through a substance. It describes emitted light intensity I, as a function of incident intensity I_0, the wavelength-dependent optical extinction coefficient ε, path length of the light l, and concentration of the substance $[C]$.

$$I = I_0 e^{-\varepsilon_\lambda [C] l} \tag{A.2}$$

When light is shone through the finger, there are many tissues with different path

lengths, concentrations and extinction coefficients contributing to the light attenuation. The right hand side of this equation can be split into components: attenuation due to arterial Hb, attenuation due to arterial HbO_2, and attenuation due to other tissues. Their contributions to the overall light extinction is assumed to be additive.

This equation applies between pulses of arterial blood, at the trough of the PPG signal (I_t). l_b is the path length through the arterial blood, and l_{tissue} is the path length through other tissues.

$$I_t = I_0 e^{-\varepsilon_{tissue}[tissue]l_{tissue} - \varepsilon_{Hb}[Hb]l_b - \varepsilon_{HbO2}[HbO_2]l_b} \tag{A.3}$$

A.2 Isolation of Absorption Due to Arterial Blood

Pulse oximetry uses the pulsating nature of arterial blood to isolate the Hb and HbO_2 terms. When an arterial blood pulse enters the finger, the arteries dilate and the path length through the arterial blood changes slightly (Δl). A new light absorption equation can be set up for the light attenuation at the peak of the arterial pulse (I_p).

$$I_p = I_0 e^{-\varepsilon_{tissue}[tissue]l_{tissue} - \varepsilon_{Hb}[Hb](l_b+\Delta l) - \varepsilon_{HbO2}[HbO_2](l_b+\Delta l)} \tag{A.4}$$

Dividing (A.4) by (A.3) isolates the the Hb and HbO_2 terms by cancelling out the effects of other tissues and the power of the incident light.

$$ln(I_p/I_t) = \varepsilon_{Hb}[Hb]\Delta l + \varepsilon_{HbO2}[HbO_2]\Delta l \tag{A.5}$$

A.3 Obtaining R and SpO_2

The dependence on Δl needs to be eliminated. Since extinction coefficients ε_{Hb} and ε_{HbO2} are functions of the incident wavelength, changing the incident wavelength produces a new equation. Typically, red and infrared wavelengths are used. The next step is calculation of the R parameter, which is obtained by dividing (A.5) by the corresponding equation using another wavelength of light. Subscripts R and IR represent red and infrared wavelengths.

$$R = \frac{ln(I_p/I_t)_{Red}}{ln(I_p/I_t)_{IR}} = \frac{\varepsilon_{Hb,Red}[Hb] + \varepsilon_{HbO2,Red}[HbO_2]}{\varepsilon_{Hb,IR}[Hb] + \varepsilon_{HbO2,IR}[HbO_2]} \tag{A.6}$$

Combining (A.6) and (A.1) yields the relationship between R and SpO_2.

$$SpO_2 = \frac{\varepsilon_{Hb,Red} - \varepsilon_{HbO2,Red}R}{\varepsilon_{Hb,Red} - \varepsilon_{HbO2,Red} + (\varepsilon_{HbO2,Red} + \varepsilon_{Hb,IR})R} \tag{A.7}$$

Because each of the extinction coefficients (ε) is a constant at a specific wavelength of light, the relation in (A.7) can be used to calculate SpO_2 directly. In practice however, R values are mapped to SpO_2 values using empirical calibration. This is because the ε values are functions of wavelength, and manufacturing tolerances in the LEDs will cause these numbers to vary.

A.4 Alternate Form of R

Since $I_p - I_t$ is the AC PPG amplitude, R can alternatively be described as the ratio of the AC components of the red and infrared PPGs, normalized by the DC components (A.8).

$$R = \frac{ln(I_p/I_t)_{Red}}{ln(I_p/I_t)_{IR}} = \frac{AC_{Red}/DC_{Red}}{AC_{IR}/DC_{IR}} \tag{A.8}$$

Appendix B

SQI Scores for Motion Contaminated Signals

Chapter 6 proposes three automatic signal quality assessment algorithms. These algorithms produce a single SQI value for each second of pulse oximeter data.

The mean and standard deviation SQIs for each subject in each movement condition are reported in the tables below. Results for SQI_{XCORR}, SQI_{AMB} and SQI_{RICORR} are reported in Tables B.1, B.2 and B.3 respectively.

Table B.1: Mean and standard deviation of SQI_{XCORR} scores

Subject	No Motion		Low		Medium		High	
	$\bar{x}$	s	$\bar{x}$	s	$\bar{x}$	s	$\bar{x}$	s
1	0.97	0.09	0.86	0.21	0.93	0.14	0.89	0.13
2	0.95	0.10	0.89	0.16	0.76	0.13	0.76	0.12
3	1.00	0.05	0.86	0.15	0.91	0.11	0.84	0.15
4	0.99	0.06	0.91	0.13	0.92	0.12	0.84	0.12
5	1.02	0.03	0.94	0.10	0.91	0.13	0.87	0.10

Table B.2: Mean and standard deviation of SQI_{AMB} scores

Subject	No Motion		Low		Medium		High	
	$\bar{x}$	s	$\bar{x}$	s	$\bar{x}$	s	$\bar{x}$	s
1	29.2	3.1	20.6	3.8	18.0	3.3	13.6	2.7
2	33.2	1.9	20.3	3.9	20.9	4.1	22.7	3.8
3	29.7	2.7	6.9	3.7	8.9	3.3	9.6	3.5
4	14.8	2.5	5.2	4.1	8.1	3.4	-1.0	3.4
5	20.4	3.1	3.9	4.5	5.0	3.3	3.3	3.3

Table B.3: Mean and standard deviation of SQI_{RICORR} scores

Subject	No Motion		Low		Medium		High	
	$\bar{x}$	s	$\bar{x}$	s	$\bar{x}$	s	$\bar{x}$	s
1	0.9994	0.0003	0.9983	0.0019	0.9953	0.0036	0.9936	0.0044
2	0.9993	0.0002	0.9991	0.0006	0.9994	0.0005	0.9986	0.0015
3	0.9991	0.0004	0.9946	0.0104	0.9340	0.1946	0.9918	0.0104
4	0.9979	0.0014	0.9974	0.0027	0.9971	0.0021	0.9760	0.0159
5	0.9985	0.0004	0.9975	0.0028	0.9963	0.0035	0.9854	0.0434